

# Precise Holographic Manipulation of Olfactory Circuits Reveals Coding Features Determining Perceptual Detection

## Highlights

- Perceptual detection of neural stimulation probed by two-photon holographic optogenetics
- Mice can reliably detect single action potentials across <20 olfactory bulb neurons
- Detection depends strongly on neuronal synchrony, but not latency relative to inhalation

## Authors

Jonathan V. Gill, Gilad M. Lerman, Hetince Zhao, Benjamin J. Stetler, Dmitry Rinberg, Shy Shoham

## Correspondence

rinberg@nyu.edu (D.R.),  
shoham@nyu.edu (S.S.)

## In Brief

Using two-photon holographic optogenetics, Gill, Lerman et al. show that mice can reliably detect single spikes across small sets of targeted olfactory bulb neurons. They find that detection performance depends strongly on neuronal synchrony, but not on latency relative to inhalation.

Article

# Precise Holographic Manipulation of Olfactory Circuits Reveals Coding Features Determining Perceptual Detection

Jonathan V. Gill,<sup>1,2,6</sup> Gilad M. Lerman,<sup>1,6</sup> Hetince Zhao,<sup>1,3</sup> Benjamin J. Stetler,<sup>1,3</sup> Dmitry Rinberg,<sup>1,2,4,\*</sup> and Shy Shoham<sup>1,3,5,7,\*</sup>

<sup>1</sup>Neuroscience Institute, New York University Langone Health, New York, NY 10016, USA

<sup>2</sup>Center for Neural Science, New York University, New York, NY 10003, USA

<sup>3</sup>Tech4Health Institute, New York University Langone Health, New York, NY 10016, USA

<sup>4</sup>Department of Physics, New York University, New York, NY 10003, USA

<sup>5</sup>Department of Ophthalmology, New York University Langone Health, New York, NY 10016, USA

<sup>6</sup>These authors contributed equally

<sup>7</sup>Lead Contact

\*Correspondence: [rinberg@nyu.edu](mailto:rinberg@nyu.edu) (D.R.), [shoham@nyu.edu](mailto:shoham@nyu.edu) (S.S.)

<https://doi.org/10.1016/j.neuron.2020.07.034>

## SUMMARY

Sensory systems transform the external world into time-varying spike trains. What features of spiking activity are used to guide behavior? In the mouse olfactory bulb, inhalation of different odors leads to changes in the set of neurons activated, as well as when neurons are activated relative to each other (synchrony) and the onset of inhalation (latency). To explore the relevance of each mode of information transmission, we probed the sensitivity of mice to perturbations across each stimulus dimension (i.e., rate, synchrony, and latency) using holographic two-photon optogenetic stimulation of olfactory bulb neurons with cellular and single-action-potential resolution. We found that mice can detect single action potentials evoked synchronously across <20 olfactory bulb neurons. Further, we discovered that detection depends strongly on the synchrony of activation across neurons, but not the latency relative to inhalation.

## INTRODUCTION

Animals are capable of detecting minute sensory stimuli. For mice, who rely on olfaction to navigate the world, each respiration leads to an influx of volatile chemical molecules entering the nose, any of which may provide important information about the environment. After binding to receptors in the olfactory epithelium, odor information is conveyed to cortical and subcortical regions from the olfactory bulb exclusively through ~50,000 projecting mitral and tufted cells (MTCs). Strikingly, MTCs altogether continuously generate  $10^5$ – $10^6$  action potentials per second, even in the absence of an odor (Cury and Uchida, 2010; Shusterman et al., 2011; Arneodo et al., 2018). Yet rodents are capable of detecting odorants in a single sniff, at extremely low concentrations (as low as  $10^{-12}$  M), despite this strong spontaneous activity (Uchida and Mainen, 2003; Rinberg et al., 2006; Dewan et al., 2018). This ability, which is crucial for survival, permits the detection of vital cues (for example, a distant food source or a hiding predator) in less than 100 ms (Resulaj and Rinberg, 2015; Wilson et al., 2017). What underlies this capacity and what are the minimal features of neural activity that can convey sensory information to guide behavior (Houweling and Brecht, 2008; Huber et al., 2008; O'Connor et al., 2013; Doron et al., 2014; Histed and Maunsell, 2014)?

Within neural activity patterns, information useful for identifying a stimulus is carried by changes in spiking along several feature dimensions, including spike rates, the synchrony between neurons, and the latency of responses relative to internal or external events. In olfaction, odor inhalation augments ongoing spiking by activating specific sets of MTCs with a temporal precision of ~10 ms, at latencies that tile the sniff cycle (Cury and Uchida, 2010; Shusterman et al., 2011; Arneodo et al., 2018). Yet it is unknown which features of stimulus-evoked activity (e.g., rate, synchrony, or latency) are used to guide olfactory behaviors at the perceptual limit.

To determine which features are relevant for behavior, we need to establish causal links between specific features of neural activity and perception. This requires the ability to manipulate neural activity while monitoring behavioral readout. Using electrical and optogenetic stimulation, previous studies have revealed that rodents can detect changes in the spike rate of individual neurons (Houweling and Brecht, 2008; Doron et al., 2014; Tanke et al., 2018) or across small populations of neurons (Huber et al., 2008; Carrillo-Reid et al., 2019; Marshel et al., 2019) over 100s of milliseconds in the somatosensory and visual cortices. Other studies manipulating cortical activity have explored the role of relative spike timing (Huber et al., 2008; Histed and Maunsell, 2014) and sensitivity to latency (Yang et al., 2008; O'Connor

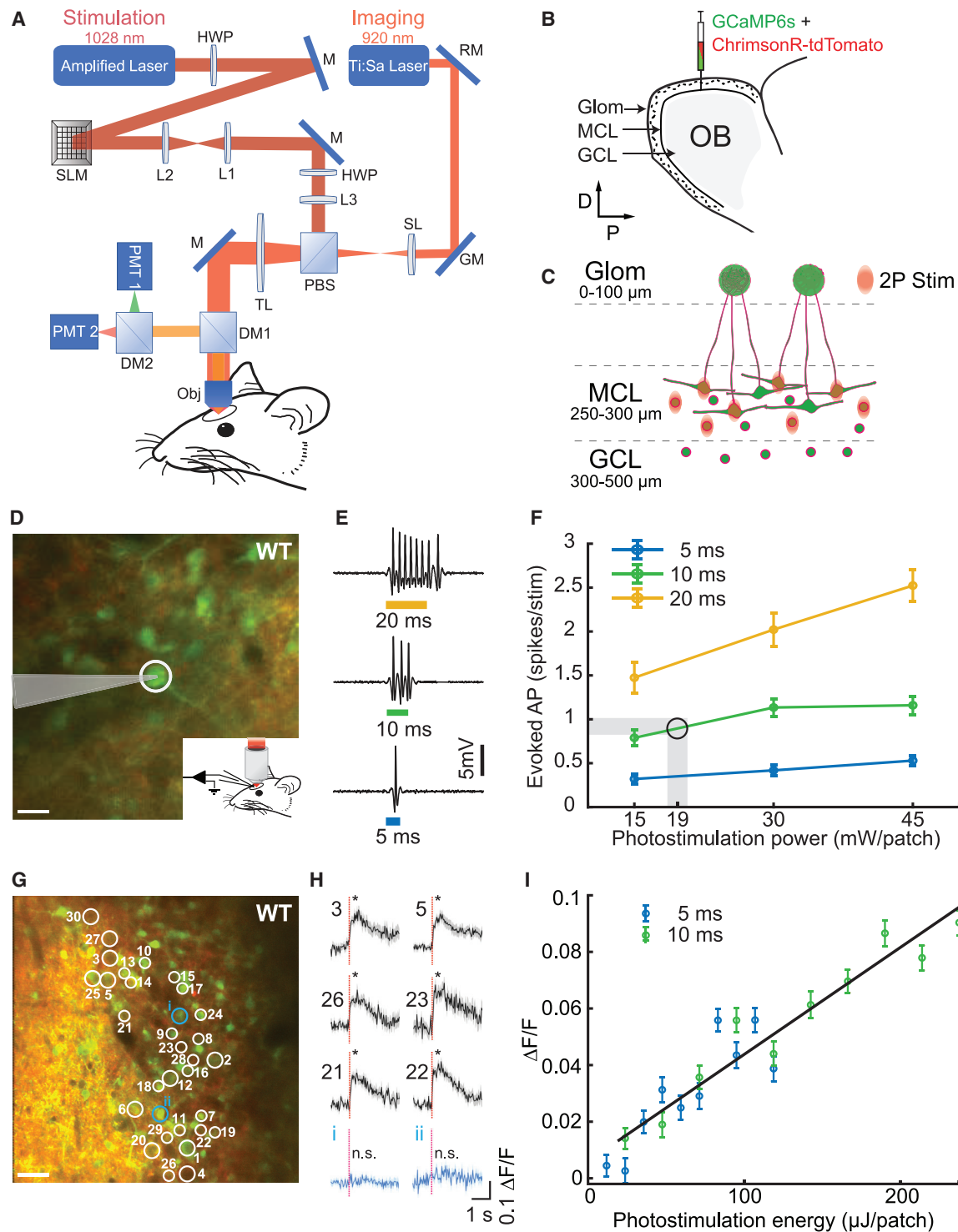


**Figure 1. All-Optical Imaging and Photostimulation**

(A) Layout of the optical system combining a 2P imaging path and scanless holographic 2P photostimulation path for experiments in a head-fixed mouse with a cranial window. DM1, DM2, dichroic mirrors; GM, galvanometer; HWP, half-wave plate; L1–L3, lenses; M, mirror; Obj, 16× objective; PBS, polarizing beamsplitter; PMT1, PMT2, photomultiplier tubes; RM, resonant mirror; SL, scan lens; SLM, spatial light modulator; TL, tube lens.

(B) Injection of viruses into the mitral cell layer (MCL) and the granule cell layer (GCL) in the olfactory bulb (OB).

(C) Schematic of 2P photostimulation patches targeted to the MCL of the OB. Large neurons, mitral cells; circles, granule cells; green, GCaMP6s; red, ChrimsonR-tdTomato.

(legend continued on next page)

et al., 2013) in populations of 100s to 1,000s of neurons. In the olfactory system, it has been demonstrated that mice can detect 10 ms optogenetic stimulation of a single glomerulus (Smear et al., 2013). However, the limits of olfactory perception at a cellular and circuit level are not yet understood. Because ~25–30 MTCs receive direct input from one glomerulus, exploring the perceptual contribution of different coding features in the minimally detectable regime requires manipulation of rate and spike timing across 10s of individual MTCs, with millisecond precision.

Holographic two-photon (2P) optogenetic photostimulation is currently the only method capable of stimulating pre-selected, distributed sets of neurons with single-cell resolution (Emiliani et al., 2015; Packer et al., 2015; Shemesh et al., 2017; Forli et al., 2018; Mardinly et al., 2018) and thus has the potential to transform the study of the behavioral relevance of specific circuits and codes (Dal Maschio et al., 2017). Indeed, this technique has recently shown promise for probing the perceptual relevance of groups of neurons in the visual system (Carrillo-Reid et al., 2019; Marshel et al., 2019). 2P optogenetic photostimulation utilizes the principle of non-linear 2P absorption to excite light-sensitive opsins within a confined axial plane (Rickgauer and Tank, 2009), permitting the specific activation of opsin-expressing neurons 100s of micrometers deep into tissue of awake animals (Rickgauer et al., 2014; Chen et al., 2019). Holographic light patterning (Nikolenko et al., 2008; Papagiakoumou et al., 2008; Golan et al., 2009) enables the simultaneously distributed activation of multiple neurons in two or three dimensions (Packer et al., 2015; Pégard et al., 2017; Accanto et al., 2018; Yang et al., 2018; Marshel et al., 2019) as well as spatially extending the excitation spot (Papagiakoumou et al., 2010; Paluch-Siegler et al., 2015; Dal Maschio et al., 2017; Shemesh et al., 2017; Mardinly et al., 2018). However, previous approaches utilizing diffraction limited spot scan to excite cells (Rickgauer et al., 2014; Packer et al., 2015; Carrillo-Reid et al., 2019; Marshel et al., 2019) lacked the temporal resolution necessary (<10 ms) to manipulate precise spike timing or reproduce the spatiotemporally patterned activity of the olfactory system. Recent technologies employing soma-covering light spots (Papagiakoumou et al., 2010; Shemesh et al., 2017; Mardinly et al., 2018; Chen et al., 2019) have the capacity for fine temporal control. Nevertheless, these have not yet been applied to probing the perceptual relevance of precise spike timing across ensembles of individual neurons.

Here, we have developed an all-optical 2P calcium imaging and photostimulation system capable of stimulating >30 neurons simultaneously in the mitral cell layer (MCL) of awake-behaving mice with single-spike resolution and millisecond precision

(millisecond jitter). This system is based on an amplified femto-second laser source capable of providing optimized optogenetic excitation of neurons expressing the red-shifted opsin ChrimsonR-tdTomato (Klapoetke et al., 2014) with relatively low average power. We used a spatial light modulator (SLM) with a 3 ms switching time for hologram generation, permitting rapid sequencing of holograms targeting different sets of neurons for the manipulation of stimulus synchrony. Critically, we simultaneously measured respiration to trigger photostimulation at a precisely defined latency from inhalation. Using this approach, we measured the detectability of artificially activated ensembles of olfactory bulb neurons while parametrically controlling spiking along one of three feature dimensions, including (1) number of cells, (2) synchrony between neurons, and (3) latency from inhalation onset.

## RESULTS

### All-Optical Imaging and Photostimulation of Olfactory Bulb Neurons

We simultaneously performed 2P holographic optogenetic photostimulation and 2P calcium imaging (Emiliani et al., 2015; Packer et al., 2015) in the olfactory bulb of awake, head-fixed mice outfitted with a cranial window (Figure 1A). To achieve high-excitation efficiency and temporal precision of photostimulation, we used an amplified laser source (1,028 nm) with low repetition rate (100s of kHz; Figure S1; Equation 1 in STAR Methods; Paluch-Siegler et al., 2015; Chaigneau et al., 2016; Ronzitti et al., 2017; Shemesh et al., 2017; Mardinly et al., 2018; Yang et al., 2018). We used a spatial light modulator (SLM) to holographically generate soma-covering light patches targeted to excitatory mitral cells (MCs) (a subset of MTCs confined to the mitral cell layer; 13- $\mu$ m-diameter light patches) and inhibitory granule cells (GCs) (10- $\mu$ m-diameter light patches; Figure S2). We used a dual viral transfection strategy to pan-neuronally express ChrimsonR-tdTomato (Klapoetke et al., 2014) together with GCaMP6s (Chen et al., 2013) in wild-type (WT) mice (Figures 1B and 1C). This approach resulted in indicator-opsin co-expression, enabling simultaneous optical photostimulation and readout (Figure S3).

To characterize the spiking response elicited by 2P photostimulation, we performed 2P guided cell-attached electrophysiological recordings (Figures 1D–1F and S4A–S4D). Photostimulation (5–20 ms duration, 15–45 mW/patch, or 0.09–0.25 mW/ $\mu$ m<sup>2</sup> at objective output) of an individual cell evoked a short latency spiking epoch with spike count dependent both on stimulation duration and power (Figures 1E and 1F). For 30 mW/patch

(D) 2P guided cell-attached electrophysiological recording in an awake WT mouse MCL co-expressing ChrimsonR-tdTomato (red) and calcium indicator GCaMP6s (green). The cell (white circle) was targeted by a light patch (scale bar, 20  $\mu$ m).

(E) Examples of electrophysiological recordings during 5, 10, and 20 ms photostimulation.

(F) Average number of evoked spikes as a function of power per cell for different stimulation durations (mean  $\pm$  SEM; n = 5 cells in 5 WT mice). Shaded area and circle indicate the working zone chosen to elicit  $\leq 1$  evoked action potential (19  $\pm$  1 mW/patch).

(G) Thirty neurons were targeted for simultaneous 2P photostimulation (white circles) and 2P imaging (scale bar, 40  $\mu$ m).

(H) Average GCaMP6s fluorescence response to photostimulation (red dashed line, stimulation onset) for 30 targeted cells (6 examples; black) and 2 example non-targeted cells (blue) for an example WT mouse (mean  $\Delta$ F/F  $\pm$  SEM; \*p < 0.05; two-sample t test; 30 trials; 10 ms stimulation duration; 0.1 mW/ $\mu$ m<sup>2</sup>; 18 mW/patch; additional data in Figure S5).

(I) Average evoked fluorescence response as a function of photostimulation energy for 5 and 10 ms durations (mean  $\Delta$ F/F  $\pm$  SEM; 20 cells; 40 trials/data point; n = 1 WT mouse).

average stimulus power, the spike count increased monotonically from  $0.41 \pm 0.06$  spikes for a 5 ms stimulation duration to  $2.02 \pm 0.19$  for 20 ms stimulation duration (Figure 1F). For a fixed stimulation duration of 10 ms, a power increase from 15 to 45 mW/patch led to an increasing number of spikes from  $0.79 \pm 0.09$  to  $1.15 \pm 0.10$  (Figures 1F and S4A). The average latency for 10 ms, 30 mW photostimulation was 5.1 ms with a jitter of 2.3 ms ( $n = 5$  cells, 119 photostimulations; jitter, SD of latencies across repetitions) and stayed below 6.9 ms latency and 3.6 ms jitter for all power-time combinations, confirming rapid and temporally precise optogenetic stimulation (Figures S4B and S4C). For the behavioral experiments described below, we chose the stimulation parameters 10 ms and 18–20 mW/patch, which on average elicited ~1 extra spike over the tonic baseline activity (Figure 1F;  $0.9 \pm 0.1$  spikes per stimulation).

We next verified that moving the photostimulation patch away from the cell's soma, both in the x-y plane ( $n = 4$  cells, 25 photostimulations per condition) and along the z axis ( $n = 9$  cells, 15 photostimulations per condition), ceased spiking activity, confirming minimal off-target excitation (Figures S4D and S4E), though lateral and axial confinement could potentially be further improved with new targeting strategies (Baker et al., 2016; Pérgard et al., 2017; Shemesh et al., 2017; Mardinly et al., 2018). Measurements of photostimulation response as a function of translation in the z axis were performed all optically using GCaMP6s fluorescence. To ensure that we could measure a robust response from all targeted cells despite differences in GCaMP6s expression, we used a higher power (30 mW/patch) than used for the behavioral experiments (18–20 mW/patch), so these measurements represent an upper bound on axial spread of the photostimulation point spread function (PSF). Additional analyses of the specificity of photostimulation-evoked activity in MCs targeted in behavioral experiments using an all-optical approach are presented later.

Next, we tested multi-neuronal photostimulation by holographically directing light patches to 30 neurons co-expressing ChrimsonR-tdTomato and GCaMP6s while recording fluorescence changes (30 trials;  $n = 3$  WT mice; Figures 1G–1I; one example field of view [FOV]). We were capable of stimulating 30 simultaneously targeted neurons (Figures 1H and S5, black traces;  $p < 0.05$ ; two-sample t test) while avoiding activation of nearby non-targeted neurons (Figures 1H and S5, blue traces;  $p \geq 0.05$ ; two-sample t test). To further test our ability to control the number of activated neurons during multi-neuronal photostimulation, we systematically omitted individual targeted neurons from multi-neuron holograms and compared the responses of each neuron when it was targeted versus when it was omitted (Figure S6A). We found a significant reduction in the response of omitted neurons in the 100 ms following photostimulation during simultaneous photostimulation of nearby targeted neurons (Figure S6B;  $p < 0.01$ ; two-sample t test;  $n = 2$  WT mice). Because omitted neurons were significantly less activated than when they were targeted, this demonstrated that multi-neuronal photostimulation was specific to targeted neurons and confirmed our ability to control the number of targeted neurons responding to photostimulation. We also observed that target responses increased with photostimulation energy in a graded manner (Figure 1I). In an example set of neurons simultaneously

photostimulated, using 5 and 10 ms durations, we found that GCaMP6s responses were dependent on photostimulation duration and increased monotonically with overall energy (20 neurons, 40 trials/energy level, and 800 photostimulations total;  $n = 1$  WT mouse). Taken together, these results demonstrated our ability to holographically target and selectively photostimulate multiple neurons simultaneously within the MCL and confirm the activation of responsive neurons using an optical readout that is sensitive to the magnitude of the response.

### Behavioral Detection of Cellular-Level Photostimulation

Having established these photostimulation capabilities, we first addressed the question of the behavioral sensitivity of mice to the number of neurons targeted for photostimulation. We trained mice to detect precisely timed photostimulation targeted to sets of individual neurons (Figure 2). Water-deprived, head-fixed mice were first trained to detect broad 1-photon optical stimulation (105- $\mu$ m-diameter optic fiber coupled to 473 nm laser) of their olfactory bulb in a go/no-go paradigm (Figures 2A and 2B). Respiration was monitored, allowing photostimulation delivery to be timed to a particular respiratory phase (20 ms after inhalation onset for WT mice; 40 ms for Tbet-cre mice) in a closed-loop manner. Mice reported detection of the stimulus by licking for a water reward (Figure 2C, top right inset) and withheld licking on trials without stimulation to avoid a punishment (5 s time-out; Figure 2C, bottom right inset). Over the course of several sessions, laser power and duration were reduced 2,500-fold in an adaptive manner while maintaining high detection accuracy (>75% correct [(hits + correct rejects)/total trials],  $n = 6$  mice, 3 WT and 3 Tbet-cre; Figures 2D and S7A). We then transitioned mice to 2P stimulation targeted to a specific subset of 30 neurons (30 holographic patches; Figures 2C and 2D). To evoke, on average, a single spike in each targeted neuron, we chose specific parameters of stimulation based on the electrophysiological recordings (Figure 1F); the stimulation duration: 10 ms and power:  $19 \pm 1$  mW/patch. For WT mice, we targeted putative MCs and GCs (~15 MCs + ~15 GCs), selected based on (1) the size of the cell soma (>20  $\mu$ m diameter for MCs;  $\leq 10$   $\mu$ m for GCs; Nagayama et al., 2014), (2) co-expression of the opsin and indicator, and (3) a significant response to photostimulation across blocks and sessions (Figure S8). Mice learned to perform the task with high accuracy over several sessions ( $6.7 \pm 2$  sessions [mean  $\pm$  SD]; 400–600 trials per session;  $n = 3$  WT mice; Figures 2D and S7B). We observed a decrease in sniff duration in the sniffs following photostimulation (data not shown), which was consistent with previous findings that rodents are capable of modulating the first sniff during odor exposure (Wesson et al., 2008; Wachowiak, 2011). There was little variability in neuronal responses to photostimulation across days, ruling out changes in performance related to virus expression, sensitization, or other non-behavioral factors influencing the efficacy of responses (Figure S8).

We further explored this sensitivity by testing detection accuracy while parametrically varying the number of targeted neurons (i.e., the number of holographic patches). For stimuli, we generated holograms targeting subsets of neurons from the original 30 neuron patterns while maintaining the same average power per holographic patch (0–30 targeted neurons;  $19 \pm 1$  mW/patch).

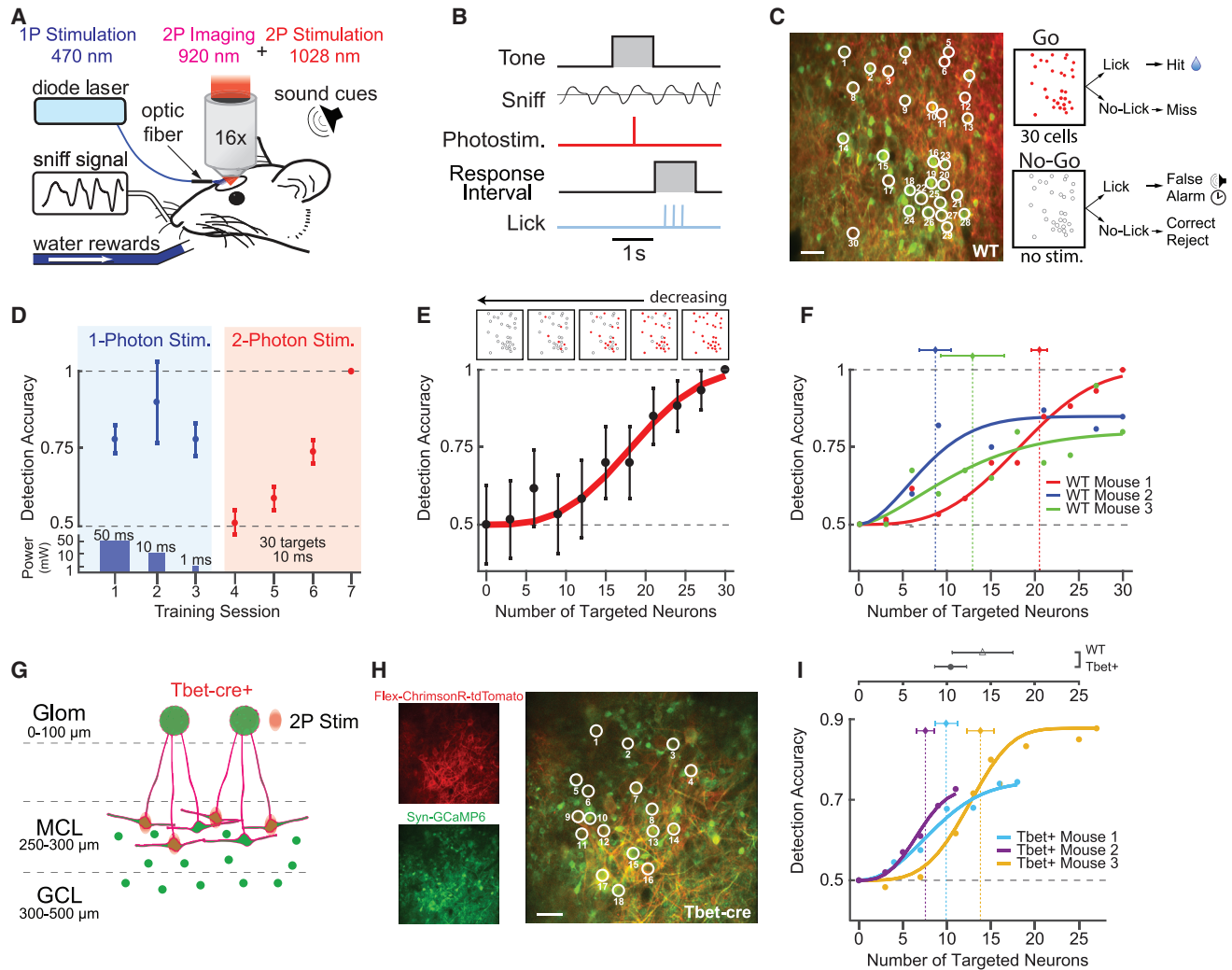


**Figure 2. Behavioral Detection of Cellular-Level Photostimulation**

(A) Schematic of photostimulation detection experiment. A head-fixed mouse with a chronically implanted window above the olfactory bulb is positioned in front of a lickspout and pressure sensor to monitor respiration (sniff). Neurons were stimulated with either 1-photon blue light (473 nm) generated by a diode laser or the 2P holographic system.

(B) Trial structure for detection experiment.

(C) Left: neurons in the mitral cell layer (MCs and GCs) co-expressing ChrimsonR-tdTomato (red) and GCaMP6s (green). Thirty neurons were targeted for simultaneous photostimulation (white circles). Scale bar, 40  $\mu\text{m}$ . Right: outcomes for responses to the “go” and “no-go” trials are shown. Red circles indicate stimulation of a particular cell, and empty circles indicate no stimulation.

(D) Representative session-by-session detection accuracy for 1P photostimulation (blue background) with decreasing power and duration of the stimulation (bottom panel), followed by 2P photostimulation of the same 30 targeted cells (pink background; mean  $\pm$  95% confidence intervals;  $n = 1$  mouse; 18 mW/patch; 0.1 mW/ $\mu\text{m}^2$  intensity). See also Figure S7.

(E) Bottom: example detection accuracy for 2P photostimulation as a function of the number of targeted neurons, fit with a psychometric function (mean  $\pm$  95% confidence intervals; 60 trials per data point;  $n = 1$  mouse; 0.1 mW/ $\mu\text{m}^2$  intensity). Top: schematic of target stimuli used in the experiment.

(F) Detection accuracy and threshold estimates across WT mice (30–60 trials/data point;  $n = 3$  WT mice; vertical dotted lines are Weibull threshold parameter fits  $\pm$  bootstrapped 95% confidence intervals).

(G) Schematic of 2P photostimulation and ChrimsonR-tdTomato expression targeted to MCs in Tbet-Cre mice. Large neurons, mitral cells; circles, granule cells; green, GCaMP6s; red, ChrimsonR-tdTomato.

(H) Left: single-channel-average images demonstrating ChrimsonR-tdTomato expression limited to a subset of MCs and GCaMP6s expression across a broad population of MCL (MCs and GCs) neurons. Right: nineteen MCs were targeted for 2P photostimulation (white circles). Scale bar, 40  $\mu\text{m}$ .

(I) Detection accuracy and threshold estimates across Tbet-cre mice (60–180 trials/data point;  $n = 3$  Tbet-cre mice; vertical dotted lines are Weibull threshold parameter fits  $\pm$  bootstrapped 95% confidence intervals). Top: comparison of mean threshold in WT and Tbet-cre mice is shown (mean  $\pm$  SEM;  $p = 0.4$ ; two-sample  $t$  test).

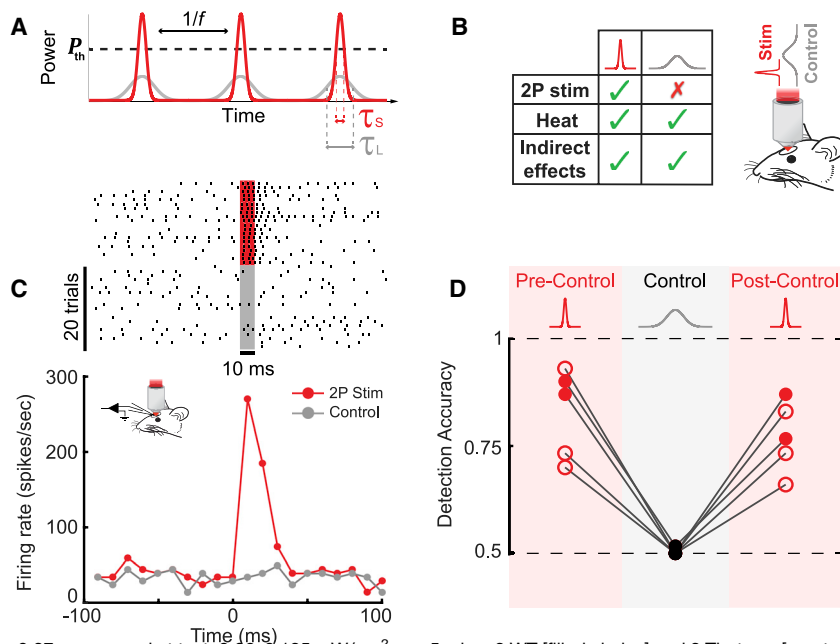


**Figure 3. Testing Necessity of Spiking for Detection Using a Pulse-Duration-Based Control**

(A) A schematic demonstrating the effect of tuning the laser pulse duration. Time dependence of laser power for pulse trains with the same pulse frequency ( $f$ ) and average power but different pulse durations: short pulse,  $\tau_S$  (red) and long pulse,  $\tau_L$  (gray). To photostimulate a cell, laser power must exceed a certain threshold,  $P_{th}$ .

(B) Left: a table summarizing the differences in effects evoked by the short- and long-pulse-duration stimuli. Right: a schematic of the behavioral setup for the sham photostimulation control experiment is shown. (C) Representative example raster plots (top) and peristimulus time histograms (PSTHs) (bottom) for short-pulse photostimulation ( $\sim 200$  fs, red) and long-pulse sham photostimulation (control;  $\geq 15$  ps, gray; 20 trials per condition; 30 mW; 10 ms illumination;  $n = 1$  cell in 1 WT mouse). Additional analyses are presented in Figure S9.

(D) Detection accuracy as a function of photostimulation condition. During the sham photostimulation control blocks, detection accuracy dropped to chance level ( $0.5 \pm 0.003$ ; mean  $\pm$  SEM;  $p =$

0.37; one-sample t test;  $0.06\text{--}0.125$  mW/ $\mu\text{m}^2$ ;  $n = 5$  mice; 2 WT [filled circles] and 3 Tbet-cre [empty circles]) and was significantly different from both pre- and post-control measurements ( $p < 0.001$ ; Fisher's exact test;  $0.06\text{--}0.125$  mW/ $\mu\text{m}^2$ ;  $n = 5$  mice; 2 WT [filled circles] and 3 Tbet-cre [empty circles]).

Detection accuracy varied monotonically as a function of the number of neurons targeted (Figure 2E). Different mice exhibited different degrees of sensitivity, with threshold performance varying from  $8.7 \pm 1.8$  targeted neurons (holographic patches) at the minimum to  $20 \pm 0.9$  at the maximum (maximum likelihood estimate Weibull fits  $\pm$  SEM of bootstrap analysis; Figure 2F). Together, these data suggest that mice are exquisitely sensitive to the synchronous,  $\sim$ single-spike activation induced by  $<20$  holographic patches targeted to a mixed population of olfactory bulb neurons.

To what degree does this sensitivity rely on the cell type of targeted neurons? It is likely that our stimulation affected both major cell types in the olfactory bulb, MCs and GCs. MCs can directly drive activity in downstream circuits via long-range projections to multiple cortical and subcortical areas, potentially exciting many neurons (Sosulski et al., 2011; Haddad et al., 2013). However, individual inhibitory GCs may be better positioned to influence perception by inhibiting multiple MCs simultaneously (Amson and Strowbridge, 2017), which could potentially impact an even greater population of downstream neurons via a decrease in excitation. We addressed this question by assessing the detectability of ensembles composed only of MCs using Tbet-cre mice (Haddad et al., 2013; Figures 2G–2I). In these mice, opsin expression was limited to only a subset of MTCs using the Cre-dependent expression of FLEX-ChrimsonR-tdTomato (Klapeetke et al., 2014; Figures 2G and 2H) although GCaMP6s was expressed pan-neuronally. We further targeted MCs specifically based on their location in the MCL ( $250\text{--}300$   $\mu\text{m}$  from the brain surface). Critically, in the MCL of the dorsal olfactory bulb, nearly all MCs are restricted to a monolayer. This planar geometry, as well as the exclusion of opsin expression from other cell types precluded off-target photostimulation of non-targeted somas in the axial dimension and permitted effective single-neuron resolution of stimulation. This feature allowed us to derive a direct neuron-

resolved estimate of the detection threshold for MC activity with a putative single-spike resolution (Figure 2I, bottom). We found that Tbet-cre mice were equally sensitive to photostimulation of ensembles of MCs, as compared to photostimulation targeted to mixed MC/GC populations in WT mice, with detection thresholds slightly (but not significantly) lower when only MCs were targeted (Figure 2I, top;  $10.4 \pm 1.8$  MCs versus  $14.0 \pm 3.5$  mixed MC/GC targeting holographic patches;  $p = 0.4$ ; two-sample t test;  $n = 3$  Tbet-cre mice versus  $n = 3$  WT mice). Interestingly, MC-targeted mice reached asymptotic performance at least as quickly as when mixed populations of MCs and GCs were targeted, generally reaching  $\geq 0.7$  proportion of correct responses within the first session ( $1.3 \pm 0.3$  sessions, Tbet-cre;  $3.3 \pm 1.5$  sessions, WT; mean  $\pm$  SEM; 400–600 trials per session;  $p = 0.3$ ; two-sample t test;  $n = 6$  mice; Figures S7B and S7C). This is somewhat surprising, given that, due to constraints of the MC layer geometry and sparseness of FLEX-ChrimsonR-tdTomato expression, fewer total neurons could be targeted in these animals (11–27 MCs), yet they performed at a high rate of detection from the start of training. This rapid generalization may imply that detection in both Tbet-cre and WT mice was determined by the total number of MCs activated, with a lesser, or negative, contribution from GCs.

### Mice Detect Photostimulation Using Only Evoked Spiking

To rule out the possibility that mice were responding to heat (Picot et al., 2018) or other indirect sensory stimulation (e.g., visual or tactile), we performed a novel control experiment using a modified version of the photostimulation that reproduced all features of the stimulus but did not evoke spiking (hereafter referred to as “sham” photostimulation; Figures 3A–3D). To achieve this, we increased the laser pulse duration from  $\sim 200$  fs used for effective photostimulation to  $\geq 15,000$  fs for

sham photostimulation, thereby reducing 2P excitation by two orders of magnitude (Equation 1 in [STAR Methods](#)) yet maintaining the same average power and thus all other aspects of the stimulus ([Figures 3A, 3B, and S9A](#)). We tested the ability of sham photostimulation to evoke spiking across a range of power levels and durations. Firing rate during illumination did not differ from baseline across targeted neurons for all power levels and durations ( $p = 0.99$ ; Wilcoxon rank-sum test;  $n = 4$  cells in 4 WT mice; [Figures 3C and S9B](#)), indicating that increasing the pulse duration abolished spike generation.

To test whether mice could detect the sham photostimulation, we interleaved sham photostimulation blocks during behavior sessions in fully trained animals ([Figure 3D](#)). Detection accuracy during sham photostimulation blocks dropped to chance level ( $0.5 \pm 0.003$ ; mean  $\pm$  SEM;  $p = 0.37$ ; one-sample  $t$  test;  $n = 5$  mice, 2 WT and 3 Tbet-cre), significantly below preceding blocks ( $p < 0.001$ ; Fisher's exact test;  $n = 5$  mice, 2 WT and 3 Tbet-cre), and returned to baseline levels after reverting back to short photostimulation pulses ( $p < 0.001$ ; Fisher's exact test;  $n = 5$  mice, 2 WT and 3 Tbet-cre). Additionally, to test whether the presence of sound cues (tone at trial start) had an impact on photostimulation detection accuracy, we removed sound cues in a block of probe trials for an example animal and found no effect ( $p = 0.6$ ; Fisher's exact test; 60 probe trials;  $n = 1$  Tbet-cre mouse; [Figure S10](#)). Taken together, these findings demonstrated that photostimulation detection performance was determined by the spiking of targeted neurons and not by confounding factors.

### Specificity of Photostimulation in Behavioral Experiments

To ensure that photostimulation was specific to the targeted neurons during behavior, we analyzed population responses to photostimulation of the individual MCs targeted in the experiments described above. Prior to behavioral training, individual MCs in Tbet-cre mice were photostimulated using a relatively high average power (30–45 mW/patch) in a train of three pulses (10 ms on, 10 ms off, and 50 Hz; [Figures 4A–4E](#)). Photostimulation of individual neurons led to complex dynamics across the population of neurons within the FOV ( $365 \times 365 \mu\text{m}$ ), including significant suppression of neighboring and distant neurons within 100 ms of stimulus offset ([Figures 4B and 4C](#)). We analyzed the spatial organization of population responses to photostimulation by computing a spatial heatmap of average neuronal responses centered on each of the MC targets (49 cells; 0–100 ms post-photostimulation;  $n = 2$  Tbet-cre mice; [Figure 4D](#)). This analysis was restricted to only neurons that were ChrimsonR-tdTomato positive (the majority of visible MCs). If non-targeted MCs were photostimulated due to off-target effects or dendritic excitation, one would expect to see, on average, a gradual decrease in photostimulation response moving away from the targeted neurons. Instead, we found that the average population response was dramatically reduced outside of the targeted region, demonstrating a highly specific photostimulation capability.

To what extent is the excess population response a product of weak, off-target photostimulation or synaptically mediated network effects? Population-level calcium imaging cannot easily

differentiate between off-target and network-related activations due to the limited temporal resolution (30 Hz; [Packer et al., 2015](#); [Carrillo-Reid et al., 2016](#); [Mardinly et al., 2018](#); [Yang et al., 2018](#)). However, because GCaMP6s was expressed pan-neuronally, although FLEX-ChrimsonR-tdTomato was restricted to a subset of MCs, we could compare the response of opsin-positive neurons with opsin-negative neurons, which could only be activated through network mechanisms. To determine whether opsin-expressing neurons neighboring stimulation targets were driven above levels expected by network-related activation, we compared the response of opsin-positive (ChrimsonR+) and opsin-negative (ChrimsonR-) neurons (including putative mitral and granule cells) at eccentricities radiating from the targeted MCs when either single or multiple MCs were targeted ([Figures 4E and S12](#)). A schematic comparison of the expected result if population responses were dominated by either (1) off-target photostimulation of opsin-positive neurons or (2) network recruitment of both opsin-positive and opsin-negative neurons is outlined in [Figure S11](#). When single cells were targeted, we found that neighboring ChrimsonR+ neurons responded at a small fraction of the level of directly targeted neurons ( $0.30 \pm 0.02$ ; mean  $\pm$  SEM; 14–29  $\mu\text{m}$  from the target; 72 neurons;  $n = 2$  Tbet-cre mice; [Figure 4E](#)). Importantly, this value was not significantly different from the response of ChrimsonR- neurons at the same distance ( $0.37 \pm 0.04$ ; mean  $\pm$  SEM; 14–29  $\mu\text{m}$  from the target;  $p = 0.11$ ; two-sample  $t$  test; Holm-Bonferroni corrected for multiple comparisons; 90 neurons;  $n = 2$  Tbet-cre mice; [Figure 4E](#)). ChrimsonR+ and ChrimsonR- responses were generally not significantly different for the majority of the bins extending out from the targets. Similarly, when multiple MCs (11–27) were targeted, we again found that the median Chrimson+ response did not systematically exceed that of the ChrimsonR- response across the field of view (ChrimsonR+: 0.013 median, 0.011–0.016 95% confidence interval [CI], versus ChrimsonR-: 0.017 median, 0.015–0.021 95% CI;  $p = 0.06$ ; Wilcoxon rank-sum test; 183 Chrimson+ and 369 Chrimson- neurons;  $n = 3$  Tbet-cre mice; [Figure S12A](#)), even in the neurons closest to the targeted MCs (ChrimsonR+: 0.018 median, 0.012–0.029 95% CI, versus ChrimsonR-: 0.016 median, 0.011–0.021 95% CI;  $p = 0.32$ ; Wilcoxon rank-sum test; 14–25  $\mu\text{m}$  from targeted MCs; 56 Chrimson+ and 136 Chrimson- neurons;  $n = 3$  Tbet-cre mice; [Figure S12B](#)).

Taken together, these results demonstrated that photostimulation was highly specific to the MCs targeted during the behavioral experiments utilizing MC-specific opsin expression. Although we cannot definitively preclude off-target stimulation, this evidence strongly suggests (1) responses in opsin-positive neurons that were not directly targeted were generally a small fraction of those that were targeted and (2) that any residual response observed  $>15 \mu\text{m}$  away from directly targeted neurons is likely to have been generated by network (i.e., synaptic) activity and not direct activation of opsin-expressing neurons.

### Behavioral Detection Depends on the Synchrony of Evoked Spikes

Next, we tested the dependence of detection sensitivity on the synchrony of activation in targeted MCs. To manipulate

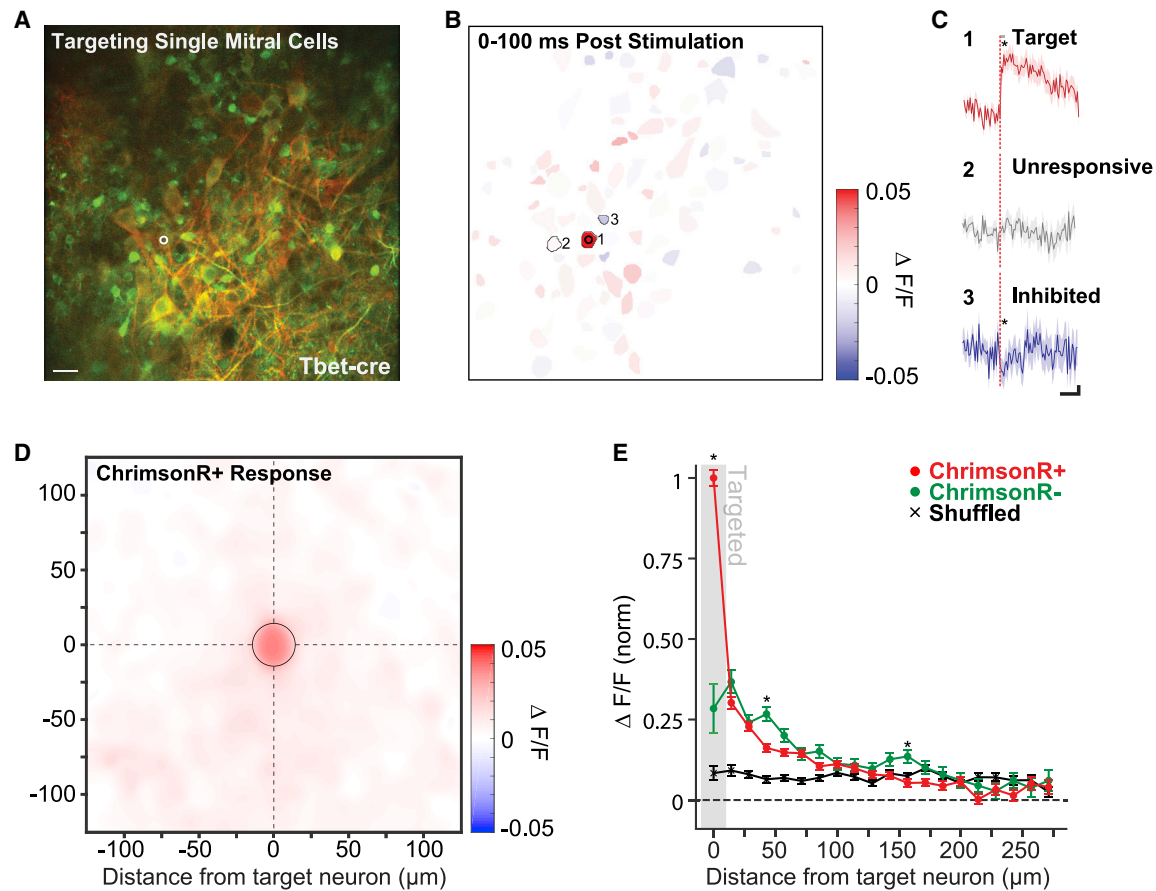


**Figure 4. Specificity of Photostimulation-Evoked Activity**

(A) Example FOV centered on the mitral cell layer of a Tbet-cre mouse. One mitral cell is targeted for 2P photostimulation (white circle, 15  $\mu\text{m}$  diameter). Red labeling corresponds to FLEX-ChrimsonR-tdTomato expression limited to a subset of mitral cells, and green labeling corresponds to pan-neuronal GCaMP6s expression. Scale bar, 40  $\mu\text{m}$ .

(B) Segmented regions of interest (ROIs) from the same FOV as (A) colored by mean evoked response to photostimulation (3 pulses: 10 ms on–10 ms off at 30 mW or 0.19  $\text{mW}/\mu\text{m}^2$ ; 60 photostimulations) of the targeted mitral cell (cell 1).

(C) The response to photostimulation of 3 example cells: cell 1, the target neuron; cell 2, neighboring unresponsive neuron; and cell 3, neighboring inhibited neuron (solid lines and shading are mean  $\pm$  SEM; 60 photostimulations; \* $p < 0.05$ ; two-sample t test). Significance of modulation following photostimulation was computed by comparing mean activity in a 100-ms window following the offset of photostimulation (gray bar) to mean activity in a 100-ms window prior. Scale bar values are 500 ms horizontal and 0.01 df/f vertical.

(D) A spatial heatmap of average response versus ROI position centered on 49 MC targets ( $n = 2$  Tbet-cre mice, 138 total neurons, 3,631 photostimulations). Only cells labeled with ChrimsonR-tdTomato were included. The “targeted” bin is outlined by a black circle.

(E) The average radial decay of responses across ChrimsonR-tdTomato-positive neurons (red) and ChrimsonR-tdTomato-negative neurons (green). Cell responses were averaged within 14  $\mu\text{m}$  (20 pixel) bins radiating out from each targeted neuron, and bin means were averaged across targets (mean  $\pm$  SEM; 49 targeted neurons;  $n = 2$  Tbet-cre mice). Shuffled data correspond to the average binned responses of the same neurons with stimulation times randomly chosen (see STAR Methods). Asterisks indicate a significant difference between the average binned response of ChrimsonR+ and ChrimsonR– neurons (\* $p < 0.05$ ; two sample t test; Holm-Bonferroni corrected for multiple comparisons).

synchrony, in blocks of probe trials, we divided the ensemble of targeted neurons into two or three smaller groups of neurons and photostimulated them sequentially. Each group was photostimulated for 10 ms, with a 10-ms inter-group interval. In this way, we could de-synchronize the neural activity evoked by photostimulation and compare detection accuracy to the synchronous case where the whole ensemble was photostimulated at once. We divided the full stimulus hologram into two or three holograms, each targeting half or a third of the neurons randomly chosen from the initially targeted population, keeping the average po-

wer per targeted neuron constant (20–25  $\text{mW}/\text{patch}$ ; Figure 5A). The photostimulation interval for all trials was centered at 45-ms latency from the onset of inhalation. Thus, we changed the synchrony, or the effective time spread, of evoked activity by changing the total photostimulation time span (stimulus spread) from 10 ms (1 group) to 30 ms (2 groups) and 50 ms (3 groups) while keeping constant the total number of photostimulated cells, photostimulation efficiency for each individual cell, and the average spike latency from inhalation onset. We found that detection decreased to near-chance performance after increasing the

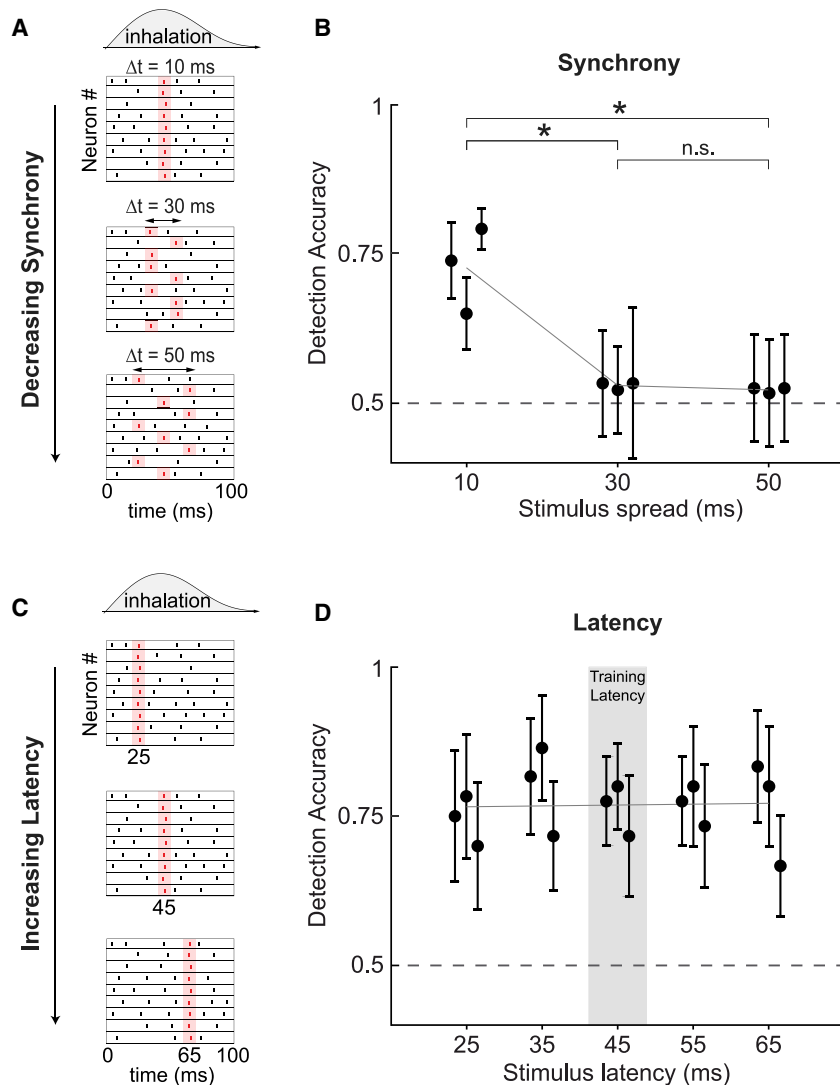


**Figure 5. Behavioral Performance as a Function of Synchrony and Latency**

(A) Schematic of stimuli that vary in the synchrony across neurons, but not the total evoked spike count. Stimuli were presented with a mean latency of 45 ms across conditions.

(B) Detection accuracy as a function of stimulus spread (mean  $\pm$  95% confidence intervals; \* $p < 0.05$ ; Fisher's exact test; 0.125–0.156 mW/ $\mu\text{m}^2$ ; 20–25 mW/patch; 11–27 cells/mouse; 120 trials/data point;  $n = 3$  Tbet-cre mice).

(C) Schematic of stimuli that vary in the latency of photostimulation relative to the onset of inhalation, but not synchrony.

(D) Detection accuracy as a function of stimulus latency for synchronous stimuli (mean  $\pm$  95% confidence intervals; best fit line;  $0.0001 \pm 0.0016$ ; slope  $\pm$  95% CI;  $p = 0.75$ ; Kruskal-Wallis ANOVA; 0.125–0.156 mW/ $\mu\text{m}^2$ ; 20–25 mW/patch; 11–27 cells/mouse; 120 trials/data point;  $n = 3$  Tbet-cre mice).

responding to evoked spiking around the 45-ms latency used for behavioral shaping. This also serves as an important control, clearly dissociating between the effects of latency and synchrony and ruling out possible differences in sensitivity across this latency range as driving the decrease in performance observed when synchrony was degraded.

## DISCUSSION

In this work, we developed and applied a methodology for 2P photostimulation of individual neurons in the MCL of the olfactory bulb to explore the sensitivity limits of detection at the scale of single neurons and spikes. Putative single spikes in completely artificial ensembles of a few neurons are detectable, so long as they

occur within  $<30$  ms of each other. These results indicate that synchronous spiking of MCs is an essential feature for the detection of sparse neural signals at the behavioral limit. This finding is largely consistent with a class of models for neural information transfer, which proposed that precise spatiotemporal synchronization of multi-neuron ensembles may enable sensory systems to maintain sensitivity within “noisy” backgrounds of population activity by enhancing their robustness (Abeles, 1991; Perez-Orive et al., 2002; Schneidman et al., 2006; Poo and Isaacson, 2009). Synchrony has also been posited to play an essential role in the reliable propagation of activity between circuits with strong feedforward inhibition, such as the thalamo-cortical (Tiesinga et al., 2008; Bruno, 2011) and the olfactory bulb-piriform cortex circuits (Luna and Schoppa, 2008). Parallel work has revealed that piriform cortex neurons are finely tuned to the precise timing of MTC activity (Haddad et al., 2013), so this region may be a suitable candidate for identifying the mechanisms by which downstream neurons might leverage the fine timing in the olfactory bulb for efficient information transmission.

### Behavioral Detection Does Not Depend on the Latency of Evoked Spikes

Finally, in blocks of probe trials in fully trained Tbet-cre mice, we tested each animal's ability to detect synchronous activation of the full ensemble of stimulated cells as a function of stimulation latency in the range of 25–65 ms from inhalation onset (Figure 5C). We found no significant difference in detection accuracy across latencies (Figure 5D;  $p = 0.75$ ; Kruskal-Wallis analysis of variance; 120 probe trials per latency;  $n = 3$  Tbet-cre mice). This suggests that animals are sensitive to stimuli arriving across the early inhalation window and that animals did not employ the strategy of only

occur within  $<30$  ms of each other. These results indicate that synchronous spiking of MCs is an essential feature for the detection of sparse neural signals at the behavioral limit. This finding is largely consistent with a class of models for neural information transfer, which proposed that precise spatiotemporal synchronization of multi-neuron ensembles may enable sensory systems to maintain sensitivity within “noisy” backgrounds of population activity by enhancing their robustness (Abeles, 1991; Perez-Orive et al., 2002; Schneidman et al., 2006; Poo and Isaacson, 2009). Synchrony has also been posited to play an essential role in the reliable propagation of activity between circuits with strong feedforward inhibition, such as the thalamo-cortical (Tiesinga et al., 2008; Bruno, 2011) and the olfactory bulb-piriform cortex circuits (Luna and Schoppa, 2008). Parallel work has revealed that piriform cortex neurons are finely tuned to the precise timing of MTC activity (Haddad et al., 2013), so this region may be a suitable candidate for identifying the mechanisms by which downstream neurons might leverage the fine timing in the olfactory bulb for efficient information transmission.

Consistent with the idea that the action potentials generated synchronously in small groups of targeted neurons were supra-threshold for perception, we found that mice did not require extensive training to detect small populations of simultaneously stimulated MCs (11–27 MCs in *Tbet-cre* mice) at above-chance level. Mice reached within ~10% of their peak performance within the first two training sessions when MCs alone were targeted, without the need for further perceptual learning. Notably, this generalization also extended into the temporal domain, as mice were equally sensitive across a range of latencies from inhalation, without a clear peak in performance centered on the latency used during shaping. This further suggests that mice attended to signals occurring within a broad time window during inhalation and did not limit their responses to stimuli occurring at a fixed latency learned through training.

Our approach also allowed us to study the contribution of different cell types, as we could resolve excitatory and inhibitory neurons both genetically and by their morphology. We targeted mixed ensembles of both MCs and granule cells using pan-neuronal opsin labeling in WT mice as well as ensembles composed only of MCs using MTC-specific expression in *Tbet-cre* mice. Surprisingly, we found little difference in the sensitivity of mice to 2P photostimulation as a function of targeted cell type. Previous studies have reported that electrical stimulation of inhibitory neurons in the cortex is on average more perceptible than stimulation of excitatory neurons (Doron et al., 2014). In the olfactory bulb, we found no evidence that including inhibitory neurons in targeted ensembles decreased detection thresholds or sped up training.

Our results also speak to a parallel literature that has sought to define the limits of signal detectability in the nervous system. Previous experiments have lent support to the idea that small groups of neurons may have a salient impact on perception (Houweling and Brecht, 2008; Huber et al., 2008; O'Connor et al., 2013; Doron et al., 2014; Histed and Maunsell, 2014), yet previous approaches left unclear the degree to which animals are attuned to the precise ensemble activity of sensory regions. Here, we employed genetic and holographic targeting to restrict opsin expression and photostimulation to a single layer of MCs in *Tbet-cre* mice and confirmed MC response characteristics and photostimulation specificity using both single-unit recordings and population analyses. This study provides the first direct evidence for the number of simultaneously active neurons and spikes necessary for photostimulation detection in the mouse, refining previous estimates by an order of magnitude (<30 versus  $\geq 300$ ; Huber et al., 2008).

A related series of studies employing electrical nanostimulation have established that rodents can detect spike trains evolving over ~200 ms in single cortical neurons (Houweling and Brecht, 2008; Doron et al., 2014; Tanke et al., 2018). Although conceptually relevant, the nanostimulation paradigm used in these experiments explored an essentially different regime of information processing from the present study. In the former paradigm, animals accumulated evidence (multiple spikes) over time (e.g., 200 ms) about the presence or absence of a stimulus. In the present study, an animal's response is determined by a very brief volley of information conveyed across multiple neurons. The distinction between these two modes of infor-

mation transmission is summarized in Figure S13. We would argue that the regime explored by our study is relevant for a range of behaviors that require rapid perceptual judgments. For example, Stanford et al. (2010) showed that perceptual categorization decisions in non-human primates are formed in less than 30 ms, following up on a long line of evidence for ultra-fast processing in the CNS (Thorpe and Fabre-Thorpe, 2001; Stanford et al., 2010). Moreover, recent work in the olfactory and visual systems (Wesson et al., 2008; Stanford et al., 2010; Resulaj and Rinberg, 2015; Wilson et al., 2017; Resulaj et al., 2018), have revealed that rodents make decisions about salient perceptual cues within very short (<100 ms) temporal windows. This line of evidence suggests that, for a host of behaviors, the initial volley of spikes across an ensemble (with approximately a single spike per neuron) carries the salient message, and we therefore offer our results as complementary to insights gained from nanostimulation, as well as other studies employing temporally extended photostimulation paradigms (Carrillo-Reid et al., 2019; Marshel et al., 2019).

The current study makes a critical contribution to our understanding of the constraints on information transmission at the perceptual limit. Remarkably, single spikes evoked synchronously across only a few MCs were detectable on top of the relatively high baseline firing rate of the olfactory bulb (8–25 Hz; Cury and Uchida, 2010; Shusterman et al., 2011; Arneodo et al., 2018; though see also Kollo et al., 2014). In a 10-ms time bin, MTCs spontaneously generate ~5,000 spikes, and the ability to robustly and very quickly learn to detect <1% “relevant” spikes highlights a remarkable adaptive performance characteristic of sensory systems. The technical and conceptual contribution of the approach applied here is likely to be broadly applicable to the study of other systems in which information is encoded at fine spatial-temporal scales. Future work comparing thresholds derived using this technique across sensory systems, and cell types, will help further constrain models linking ensemble activity to sensory coding.

## STAR★METHODS

Detailed methods are provided in the online version of this paper and include the following:

- KEY RESOURCES TABLE
- RESOURCE AVAILABILITY
  - Lead Contact
  - Materials Availability
  - Data and Code Availability
- EXPERIMENTAL MODEL AND SUBJECT DETAILS
  - Mouse lines
- METHOD DETAILS
  - Surgical preparation
  - Imaging and photostimulation
  - Online motion correction
  - Image processing and analysis
  - Targeted juxtacellular electrophysiology
  - Network responses to photostimulation
  - Behavioral training
  - Assessment of detection thresholds

- Manipulation of stimulus timing
- Optical sham-stimulation control
- **QUANTIFICATION AND STATISTICAL ANALYSIS**

#### SUPPLEMENTAL INFORMATION

Supplemental Information can be found online at <https://doi.org/10.1016/j.neuron.2020.07.034>.

#### ACKNOWLEDGMENTS

The authors thank G. Serrano and S. Stark for surgical assistance, C. Wilson for aid in experimental programming, E. Chong for help with behavioral training, and A. Resulaj and H. Ma for help in behavioral system design. The authors also thank G. Kosche, M. Picardo, S. Benezra, and K. Martin for assistance with juxtacellular recordings as well as E. Chong, J. Little, S. Rosen, and D. Razanski for comments on the manuscript. This work was supported by the NIH BRAIN Initiative (1U01NS090498-01; U19NS107464), and J.G. was supported by a NIH graduate training grant (T90DA043219).

#### AUTHOR CONTRIBUTIONS

D.R. and S.S. designed and initiated the study and supervised the project. J.V.G., G.M.L., D.R., and S.S. designed the experiments. J.V.G., G.M.L., and H.Z. carried out the experiments and performed the data analysis. B.J.S. performed additional analyses on the imaging data. G.M.L., J.V.G., and D.R. built the experimental system. J.V.G., G.M.L., D.R., and S.S. wrote the manuscript. All authors discussed the results.

#### DECLARATION OF INTERESTS

The authors declare no competing interests.

Received: October 1, 2018

Revised: January 15, 2020

Accepted: July 27, 2020

Published: August 24, 2020

#### REFERENCES

Abeles, M. (1991). *Corticonics: Neural Circuits of the Cerebral Cortex* (Cambridge University).

Accanto, N., Molinier, C., Tanese, D., Ronzitti, E., Newman, Z.L., Wyart, C., Isacoff, E., Papagiakoumou, E., and Emiliani, V. (2018). Multiplexed temporally focused light shaping for high-resolution multi-cell targeting. *Optica* 5, 1478–1491.

Arneodo, E.M., Penikis, K.B., Rabinowitz, N., Licata, A., Cichy, A., Zhang, J., Bozza, T., and Rinberg, D. (2018). Stimulus dependent diversity and stereotypy in the output of an olfactory functional unit. *Nat. Commun.* 9, 1347.

Arnson, H.A., and Strowbridge, B.W. (2017). Spatial structure of synchronized inhibition in the olfactory bulb. *J. Neurosci.* 37, 10468–10480.

Baker, C.A., Elyada, Y.M., Parra, A., and Bolton, M.M. (2016). Cellular resolution circuit mapping with temporal-focused excitation of soma-targeted channelrhodopsin. *eLife* 5, e14193.

Bruno, R.M. (2011). Synchrony in sensation. *Curr. Opin. Neurobiol.* 21, 701–708.

Carrillo-Reid, L., Yang, W., Bando, Y., Peterka, D.S., and Yuste, R. (2016). Imprinting and recalling cortical ensembles. *Science* 353, 691–694.

Carrillo-Reid, L., Han, S., Yang, W., Akrouh, A., and Yuste, R. (2019). Controlling visually guided behavior by holographic recalling of cortical ensembles. *Cell* 178, 447–457.e5.

Chaigneau, E., Ronzitti, E., Gajowa, M.A., Soler-Llavina, G.J., Tanese, D., Brureau, A.Y., Papagiakoumou, E., Zeng, H., and Emiliani, V. (2016). Two-photon holographic stimulation of ReaChR. *Front. Cell. Neurosci.* 10, 234.

Chen, T.W., Wardill, T.J., Sun, Y., Pulver, S.R., Renninger, S.L., Baohan, A., Schreiter, E.R., Kerr, R.A., Orger, M.B., Jayaraman, V., et al. (2013). Ultrasensitive fluorescent proteins for imaging neuronal activity. *Nature* 499, 295–300.

Chen, I.W., Ronzitti, E., Lee, B.R., Daigle, T.L., Dalkara, D., Zeng, H., Emiliani, V., and Papagiakoumou, E. (2019). *In vivo* submillisecond two-photon optogenetics with temporally focused patterned light. *J. Neurosci.* 39, 3484–3497.

Cury, K.M., and Uchida, N. (2010). Robust odor coding via inhalation-coupled transient activity in the mammalian olfactory bulb. *Neuron* 68, 570–585.

Dal Maschio, M., Donovan, J.C., Helmbrecht, T.O., and Baier, H. (2017). Linking neurons to network function and behavior by two-photon holographic optogenetics and volumetric imaging. *Neuron* 94, 774–789.e5.

Dewan, A., Cichy, A., Zhang, J., Miguel, K., Feinstein, P., Rinberg, D., and Bozza, T. (2018). Single olfactory receptors set odor detection thresholds. *Nat. Commun.* 9, 2887.

Doron, G., von Heimendahl, M., Schlattmann, P., Houweling, A.R., and Brecht, M. (2014). Spiking irregularity and frequency modulate the behavioral report of single-neuron stimulation. *Neuron* 81, 653–663.

Emiliani, V., Cohen, A.E., Deisseroth, K., and Häusser, M. (2015). All-optical interrogation of neural circuits. *J. Neurosci.* 35, 13917–13926.

Forli, A., Vecchia, D., Binini, N., Succol, F., Bovetti, S., Moretti, C., Nespoli, F., Mahn, M., Baker, C.A., Bolton, M.M., et al. (2018). Two-photon bidirectional control and imaging of neuronal excitability with high spatial resolution in vivo. *Cell Rep.* 22, 3087–3098.

Gerchberg, R.W., and Saxton, W.O. (1972). A practical algorithm for the determination of phase from image and diffraction plane pictures. *Optik (Stuttg.)* 35, 237–246.

Golan, L., Reutsky, I., Farah, N., and Shoham, S. (2009). Design and characteristics of holographic neural photo-stimulation systems. *J. Neural Eng.* 6, 066004.

Haddad, R., Lanjuin, A., Madisen, L., Zeng, H., Murthy, V.N., and Uchida, N. (2013). Olfactory cortical neurons read out a relative time code in the olfactory bulb. *Nat. Neurosci.* 16, 949–957.

Histed, M.H., and Maunsell, J.H. (2014). Cortical neural populations can guide behavior by integrating inputs linearly, independent of synchrony. *Proc. Natl. Acad. Sci. USA* 111, E178–E187.

Houweling, A.R., and Brecht, M. (2008). Behavioural report of single neuron stimulation in somatosensory cortex. *Nature* 451, 65–68.

Huber, D., Petreanu, L., Ghitani, N., Ranade, S., Hromádka, T., Mainen, Z., and Svoboda, K. (2008). Sparse optical microstimulation in barrel cortex drives learned behaviour in freely moving mice. *Nature* 451, 61–64.

Klapoetke, N.C., Murata, Y., Kim, S.S., Pulver, S.R., Birdsey-Benson, A., Cho, Y.K., Morimoto, T.K., Chuong, A.S., Carpenter, E.J., Tian, Z., et al. (2014). Independent optical excitation of distinct neural populations. *Nat. Methods* 11, 338–346.

Kollo, M., Schmaltz, A., Abdelhamid, M., Fukunaga, I., and Schaefer, A.T. (2014). ‘Silent’ mitral cells dominate odor responses in the olfactory bulb of awake mice. *Nat. Neurosci.* 17, 1313–1315.

Lerman, G.M., Little, J.P., Gill, J.V., Rinberg, D., and Shoham, S. (2019). Real-time in situ holographic optogenetics confocally unraveled sculpting microscopy. *Laser Photonics Rev.* 13, 1900144.

Luna, V.M., and Schoppa, N.E. (2008). GABAergic circuits control input-spike coupling in the piriform cortex. *J. Neurosci.* 28, 8851–8859.

Mardinly, A.R., Oldenburg, I.A., Pégard, N.C., Sridharan, S., Lyall, E.H., Chesnov, K., Brohawn, S.G., Waller, L., and Adesnik, H. (2018). Precise multimodal optical control of neural ensemble activity. *Nat. Neurosci.* 21, 881–893.

Marshall, J.H., Kim, Y.S., Machado, T.A., Quirin, S., Benson, B., Kadmon, J., Raja, C., Chibukhchyan, A., Ramakrishnan, C., Inoue, M., et al. (2019). Cortical layer-specific critical dynamics triggering perception. *Science* 365, eaaw5202.

Nagayama, S., Homma, R., and Imamura, F. (2014). Neuronal organization of olfactory bulb circuits. *Front. Neural Circuits* 8, 98.

- Nikolenko, V., Watson, B.O., Araya, R., Woodruff, A., Peterka, D.S., and Yuste, R. (2008). SLM microscopy: scanless two-photon imaging and photostimulation with spatial light modulators. *Front. Neural Circuits* 2, 5.
- O'Connor, D.H., Hires, S.A., Guo, Z.V., Li, N., Yu, J., Sun, Q.Q., Huber, D., and Svoboda, K. (2013). Neural coding during active somatosensation revealed using illusory touch. *Nat. Neurosci.* 16, 958–965.
- Osborne, J.E., and Dudman, J.T. (2014). RIVETS: a mechanical system for in vivo and in vitro electrophysiology and imaging. *PLoS ONE* 9, e89007.
- Packer, A.M., Russell, L.E., Dalgleish, H.W., and Häusser, M. (2015). Simultaneous all-optical manipulation and recording of neural circuit activity with cellular resolution in vivo. *Nat. Methods* 12, 140–146.
- Paluch-Siegler, S., Mayblum, T., Dana, H., Brosh, I., Gefen, I., and Shoham, S. (2015). All-optical bidirectional neural interfacing using hybrid multiphoton holographic optogenetic stimulation. *NeuroPhotonics* 2, 031208.
- Papagiakoumou, E., de Sars, V., Oron, D., and Emiliani, V. (2008). Patterned two-photon illumination by spatiotemporal shaping of ultrashort pulses. *Opt. Express* 16, 22039–22047.
- Papagiakoumou, E., Anselmi, F., Bègue, A., de Sars, V., Glückstad, J., Isacoff, E.Y., and Emiliani, V. (2010). Scanless two-photon excitation of channelrhodopsin-2. *Nat. Methods* 7, 848–854.
- Pégar, N.C., Mardinly, A.R., Oldenburg, I.A., Sridharan, S., Waller, L., and Adesnik, H. (2017). Three-dimensional scanless holographic optogenetics with temporal focusing (3D-SHOT). *Nat. Commun.* 8, 1228.
- Perez-Orive, J., Mazor, O., Turner, G.C., Cassenaer, S., Wilson, R.I., and Laurent, G. (2002). Oscillations and sparsening of odor representations in the mushroom body. *Science* 297, 359–365.
- Picot, A., Dominguez, S., Liu, C., Chen, I.-W., Tanese, D., Ronzitti, E., Berto, P., Papagiakoumou, E., Oron, D., Tessier, G., et al. (2018). Temperature rise under two-photon optogenetic brain stimulation. *Cell Rep.* 24, 1243–1253.e5.
- Pnevmatikakis, E.A., and Giovannucci, A. (2017). NoRMCorre: an online algorithm for piecewise rigid motion correction of calcium imaging data. *J. Neurosci. Methods* 297, 83–94.
- Pologruto, T.A., Sabatini, B.L., and Svoboda, K. (2003). ScanImage: flexible software for operating laser scanning microscopes. *Biomed. Eng. Online* 2, 13.
- Poo, C., and Isaacson, J.S. (2009). Odor representations in olfactory cortex: “sparse” coding, global inhibition, and oscillations. *Neuron* 62, 850–861.
- Resulaj, A., and Rinberg, D. (2015). Novel behavioral paradigm reveals lower temporal limits on mouse olfactory decisions. *J. Neurosci.* 35, 11667–11673.
- Resulaj, A., Ruediger, S., Olsen, S.R., and Scanziani, M. (2018). First spikes in visual cortex enable perceptual discrimination. *eLife* 7, e34044.
- Rickgauer, J.P., and Tank, D.W. (2009). Two-photon excitation of channelrhodopsin-2 at saturation. *Proc. Natl. Acad. Sci. USA* 106, 15025–15030.
- Rickgauer, J.P., Deisseroth, K., and Tank, D.W. (2014). Simultaneous cellular-resolution optical perturbation and imaging of place cell firing fields. *Nat. Neurosci.* 17, 1816–1824.
- Rinberg, D., Koulakov, A., and Gelperin, A. (2006). Speed-accuracy tradeoff in olfaction. *Neuron* 51, 351–358.
- Ronzitti, E., Conti, R., Zampini, V., Tanese, D., Foust, A.J., Klapoetke, N., Boyden, E.S., Papagiakoumou, E., and Emiliani, V. (2017). Submillisecond optogenetic control of neuronal firing with two-photon holographic photoactivation of chronos. *J. Neurosci.* 37, 10679–10689.
- Schneidman, E., Berry, M.J., 2nd, Segev, R., and Bialek, W. (2006). Weak pairwise correlations imply strongly correlated network states in a neural population. *Nature* 440, 1007–1012.
- Shemesh, O.A., Tanese, D., Zampini, V., Linghu, C., Piatkevich, K., Ronzitti, E., Papagiakoumou, E., Boyden, E.S., and Emiliani, V. (2017). Temporally precise single-cell-resolution optogenetics. *Nat. Neurosci.* 20, 1796–1806.
- Shusterman, R., Smear, M.C., Koulakov, A.A., and Rinberg, D. (2011). Precise olfactory responses tile the sniff cycle. *Nat. Neurosci.* 14, 1039–1044.
- Smear, M., Resulaj, A., Zhang, J., Bozza, T., and Rinberg, D. (2013). Multiple perceptible signals from a single olfactory glomerulus. *Nat. Neurosci.* 16, 1687–1691.
- Sosulski, D.L., Bloom, M.L., Cutforth, T., Axel, R., and Datta, S.R. (2011). Distinct representations of olfactory information in different cortical centres. *Nature* 472, 213–216.
- Stanford, T.R., Shankar, S., Massoglia, D.P., Costello, M.G., and Salinas, E. (2010). Perceptual decision making in less than 30 milliseconds. *Nat. Neurosci.* 13, 379–385.
- Tanke, N., Borst, J.G.G., and Houweling, A.R. (2018). Single-cell stimulation in barrel cortex influences psychophysical detection performance. *J. Neurosci.* 38, 2057–2068.
- Thorpe, S.J., and Fabre-Thorpe, M. (2001). Neuroscience. Seeking categories in the brain. *Science* 297, 260–263.
- Tiesinga, P., Fellous, J.M., and Sejnowski, T.J. (2008). Regulation of spike timing in visual cortical circuits. *Nat. Rev. Neurosci.* 9, 97–107.
- Uchida, N., and Mainen, Z.F. (2003). Speed and accuracy of olfactory discrimination in the rat. *Nat. Neurosci.* 6, 1224–1229.
- Wachowiak, M. (2011). All in a sniff: olfaction as a model for active sensing. *Neuron* 71, 962–973.
- Wesson, D.W., Carey, R.M., Verhagen, J.V., and Wachowiak, M. (2008). Rapid encoding and perception of novel odors in the rat. *PLoS Biol.* 6, e82.
- Wilson, C.D., Serrano, G.O., Koulakov, A.A., and Rinberg, D. (2017). A primacy code for odor identity. *Nat. Commun.* 8, 1477.
- Yang, Y., DeWeese, M.R., Otazu, G.H., and Zador, A.M. (2008). Millisecond-scale differences in neural activity in auditory cortex can drive decisions. *Nat. Neurosci.* 11, 1262–1263.
- Yang, W., Carrillo-Reid, L., Bando, Y., Peterka, D.S., and Yuste, R. (2018). Simultaneous two-photon imaging and two-photon optogenetics of cortical circuits in three dimensions. *eLife* 7, e32671.
- Zipfel, W.R., Williams, R.M., and Webb, W.W. (2003). Nonlinear magic: multiphoton microscopy in the biosciences. *Nat. Biotechnol.* 21, 1369–1377.

## STAR★METHODS

### KEY RESOURCES TABLE

REAGENT or RESOURCE	SOURCE	IDENTIFIER
Virus Strains		
AAV5-Syn-GCaMP6s-WPRE-SV40	<a href="#">Chen et al., 2013</a>	Addgene Cat # 100843-AAV5
AAV5-Syn-ChrimsonR-tdTomato	<a href="#">Klapoetke et al., 2014</a>	Addgene Cat # 59171-AAV5
AAV1-hSyn-FLEX-ChrimsonR-tdTomato	UNC Vector Core, <a href="#">Klapoetke et al., 2014</a>	N/A
Chemicals, Peptides, and Recombinant Proteins		
Potassium Gluconate	Millipore Sigma	Cat # G4500-100G
Alexa Fluor 488 Hydrazide	ThermoFisher Scientific	Cat # A10436
Alexa Fluor 594 Hydrazide	ThermoFisher Scientific	Cat # A10438
Experimental Models: Organisms/Strains		
Mouse: C57BL/6J	The Jackson Lab	JAX Stock # 000664
Mouse: B6;CBA-Tg(Tbx21-cre)1Dlc/J	<a href="#">Haddad et al., 2013</a>	Deposited in the Jackson Lab; JAX Stock # 024507
Software and Algorithms		
ScanImage	Vidrio Technologies	<a href="https://vidriotechnologies.com/scanimage">https://vidriotechnologies.com/scanimage</a>
MATLAB	MathWorks	<a href="https://in.mathworks.com/products/matlab.html">https://in.mathworks.com/products/matlab.html</a>
NoRMCorre	<a href="#">Pnevmatikakis and Giovannucci, 2017</a>	<a href="https://github.com/flatironinstitute/NoRMCorre">https://github.com/flatironinstitute/NoRMCorre</a>
ImageJ	NIH	<a href="https://imagej.nih.gov/ij/">https://imagej.nih.gov/ij/</a>
WaveSurfer	Janelia Research Campus	<a href="https://www.janelia.org/open-science/wavesurfer">https://www.janelia.org/open-science/wavesurfer</a>
Gerchberg-Saxton algorithm	<a href="#">Golan et al., 2009</a>	N/A

### RESOURCE AVAILABILITY

#### Lead Contact

Further information and requests for resources should be directed to and will be fulfilled by the Lead Contact, Shy Shoham ([shoham@nyu.edu](mailto:shoham@nyu.edu)).

#### Materials Availability

This study did not generate new unique reagents.

#### Data and Code Availability

The datasets generated and/or analyzed during the current study are available from the corresponding authors on reasonable request.

### EXPERIMENTAL MODEL AND SUBJECT DETAILS

#### Mouse lines

All procedures were approved under a New York University Langone Health institutional animal care and use committee (IACUC) protocol 161211-02. Male and female C57BL/6J mice (Stock No: 000664, Jackson Laboratories) and Tbet-Cre mice ([Haddad et al., 2013](#)) (Stock No: 024507, Jackson Laboratories) between 2 and 4 months old were used in all experiments and handled in accordance with institutional guidelines.

### METHOD DETAILS

#### Surgical preparation

Mice were anesthetized with isoflurane during viral injections and surgical implantation (2.0% during induction, 1.5% during surgery). A circular craniotomy was performed to expose both hemispheres of the dorsal olfactory bulb (3 mm craniotomy extending from the

rostral rhinal vein to the naso-frontal suture, centered on the midline) using an air-driven dental drill (Midwest Tradition, FG 1/8 drill bit). Adeno-associated viral (AAV) vectors encoding the calcium indicator GCaMP6s (AAV5-Syn-GCaMP6s-WPRE-SV40, Addgene) and red-shifted opsin ChrimsonR (AAV5-Syn-ChrimsonR-tdTomato, Addgene; or AAV1-hSyn-FLEX-ChrimsonR-tdTomato, UNC vector core) were mixed at a ratio of 1:1 and injected bilaterally using a stereotactic syringe pump (World Precision Instruments Inc.) at a rate of  $0.1 \mu\text{l min}^{-1}$  (800 nL per hemisphere, 400–600  $\mu\text{m}$  deep). Following injection, a cranial window was implanted replacing a circular piece of skull by a glass coverslip (3 mm diameter, Warner Instruments) that was secured in place using a mix of self-curing resin (Orthojet, Lang Dental) and cyanoacrylate glue (Krazy Glue). For electrophysiological recordings, the cranial window contained two  $\sim 1$  mm diameter holes pre-drilled and filled with a silicone elastomer (Kwik-Sil, World Precision Instruments). A custom 3D-printed headpost (Osborne and Dudman, 2014) was placed around the cranial window and affixed to the skull using C&B Metabond dental cement (Parkell). Each animal recovered for at least 10 days prior to experiments.

### Imaging and photostimulation

The system combined an imaging arm and a photostimulation arm to achieve all-optical two-photon imaging and photostimulation (Figure 1A). Imaging was performed on a custom multiphoton microscope system based on the MIMMS 1.0 design (HHMI Janelia Research Campus, Ashburn, VA). Two-photon fluorescence of GCaMP6s and tdTomato was excited at 920 nm using a mode locked, 80 MHz repetition rate, femtosecond-pulsed, Ti:Sapphire laser with dispersion compensation (Mai Tai eHP DS or InSightX3, Spectra-Physics, Mountain View, CA). The beam was relayed and magnified by a telescope (scan lens,  $f = 35$  mm, and tube lens,  $f = 200$  mm) to the back-aperture of a  $16 \times /0.8$ -NA water immersion objective lens (Nikon) mounted to a piezoelectric stage (P-725KHDS, Physik Instrument). Images were acquired at 30 Hz using resonant-galvanometer raster scanning (Cambridge Research). Emitted photons were reflected by a dichroic mirror (DM1, FF705-Di01, Semrock) and separated to either green or red channels via a dichroic mirror (DM2, 565dcxr, Chroma) and fluorescence was detected using GaAsP photomultiplier tubes (H10770PB-40, Hamamatsu). Images were digitized and recorded using ScanImage software (Pologruto et al., 2003) (Vidrio Technologies). The stability of the imaging and head-fixation system permitted imaging of the same FOV over multiple weeks in longitudinal experiments.

2P photostimulation was performed using an amplified femtosecond laser source (Pharos, SP-06-600-PP Light Conversion, 10 W maximal average power, 190 fs pulse width at 628 KHz repetition rate, except where noted) at 1028 nm. Because 2P excitation efficiency is inversely proportional to both the repetition rate  $f$ , and pulse width,  $\tau$ :  $2P \propto P_{\text{avg}}^2 / \tau f$  (Equation 1 (Zipfel et al., 2003), Figure S1), an amplified laser has a much stronger 2P excitation than a standard Ti:Sapphire oscillator with a frequency of  $\sim 80$  MHz and a comparable average power  $P_{\text{avg}}$ . The repetition rate and pulse duration of the laser were tunable and were used to find the optimal parameters for 2P excitation, and to change the laser's peak power for the control experiments. The beam power was controlled via the laser's software and was measured at the laser output and also after the objective lens to verify the power level hitting the brain. We controlled the internal Pockels cell of the laser with a TTL pulse and used it as the shutter for the system achieving very short  $< 1$  ms opening times not possible with a mechanical shutter. The beam was expanded with a telescope (BE02M-B, Thorlabs) to fill the SLM active area and the polarization was optimized with a half-wave plate (HWP, AHWP10M-980, Thorlabs) to achieve the best efficiency of the reflective SLM (HSPDM512-920-1110, Meadowlark Optics, optimized for 1064 nm,  $7.68 \times 7.68$  mm<sup>2</sup> active area,  $512 \times 512$  pixels). The SLM had an overdrive mode with a 3 ms refresh time which, combined with the rapid photostimulation approach outlined in this paper, allowed for stimulating with different holographic patterns in less than 10 ms. After acquiring the desired phase profile, the beam was relayed by a 1:1 telescope (L1,  $f = 100$  mm, L2,  $f = 100$  mm) to a mirror. Blocking of the zeroth diffraction order was done at the focal plane of lens L1 using a piece of aluminum foil that was glued onto a glass coverslip. An additional telescope with a  $\sim 1:3$  ratio (L3,  $f = 75$  mm, and the tube lens,  $f = 200$  mm) was used to magnify and project the beam onto the objective lens aperture. The imaging and photostimulation paths were combined by a polarizing beamsplitter cube (PBS253, 900–1300 nm, Thorlabs) and an additional HWP (AHWP10M-980, Thorlabs) was placed before the beamsplitter to rotate the polarization of the diffracted beamlets to maximize power going through the polarizing beamsplitter.

Phase masks were loaded to the SLM using the manufacturer's software development kit (SDK) and custom experimental control software written in Python. Phase calculations were performed using custom MATLAB software that made use of a modified weighted Gerchberg-Saxton (GS) algorithm (Gerchberg and Saxton, 1972; Golan et al., 2009) to optimize the intensity distribution at the focal plane. We mapped holographic efficiency across the photostimulation FOV by generating phase masks to translate a single light patch across the FOV. We measured the intensity at the objective output for each hologram and calculated the relative efficiency of the holograms as a function of position. This characterization was later used to compensate for efficiency variations as we weighted the desired intensity pattern with this efficiency map. The registration of the photostimulation FOV and the two-photon imaging FOV was performed before each experimental session to ensure precise cellular targeting. A calibration pattern was burned onto a fluorescent plate (Ted Pella, INC.) by the photostimulation system. The plate was imaged by the 2P imaging system and the calibration pattern was used for the registration of the two systems.

The point spread function (PSF) of the light patches was characterized using a widefield microscope (Figure S2). A thin ( $< 5$   $\mu\text{m}$ ) fluorescein layer was illuminated with a light patch, and the excited fluorescence signal was collected through the objective lens, the tube lens and a mirror (MGP01-350-700, Semrock) onto a CMOS camera (DCC1240M – GL, Thorlabs). The axial dimension of the photostimulation PSF was measured by generating holograms of the same light patch in different axial positions spanning the focal plane and measuring the excited fluorescence signal for each hologram. Full width at half maximum calculations for the ( $x, y$ ) and axial ( $x, z$ ) dimensions were performed after correcting for a slight tilt ( $10^\circ$ ) along the ( $x, z$ ) plane. This technique was also used

to find the effective axial resolution of the photostimulation system by measuring the GCaMP6s calcium response of targeted neurons to each axial value. These measurements used a considerably higher power per patch than was used for behavioral experiments, 30 mW/patch instead of ~19 mW/patch for behavioral detection, in order to boost signal-to-noise for optical measurements. PSF measurements could be enhanced using a new technique for real-time *in situ* evaluation of holographic light patterns, which could also account for tissue induced distortions (Lerman et al., 2019).

### Online motion correction

For behavioral experiments that required targeting the same neurons for photostimulation across days, we implemented an online motion correction method. In these experiments, the FOV was first aligned to a reference image manually, then the position was fine-tuned automatically using a custom designed closed-loop algorithm, implemented as a module within ScanImage software (Polgruto et al., 2003) (Vidrio Technologies). This algorithm attempted to minimize the difference between the reference image and the FOV by iteratively moving the microscope stage (Sutter 285) to reduce the residual displacement computed using a rigid motion correction package (NoRMCorre, Flatiron Institute (Pnevmatikakis and Giovannucci, 2017)). The optimization typically converged within 10-15s once the residual displacement vector was reduced to < 0.5  $\mu\text{m}$  in magnitude. In addition to aligning the FOV across days, we performed this routine between consecutive blocks (60 trials, 6-9 minutes) during each behavioral session to minimize the effect of slow *x-y* drift due to brain and microscope motion, therefore ensuring the photostimulation targets remained consistent throughout each session. We monitored for drift in the *z* dimension as well, which was manually corrected using the reference image between blocks (60 trials, 6-9 minutes) if necessary, though displacement was typically small (~3  $\mu\text{m}$  in a 1.5 hour session).

### Image processing and analysis

Data analysis was performed using custom-written software in ImageJ (NIH) and MATLAB (MathWorks). Images were aligned to a session-averaged template image using a non-rigid motion correction package (Pnevmatikakis and Giovannucci, 2017). Cellular regions of interest (ROIs) were manually drawn using both GCaMP6s (green) and ChrimsonR-tdTomato (red) channels, and mean fluorescence time-courses were extracted. ROI selection utilized both mean and maximum intensity projections from 3-5 blocks of trials per session (5-10 min/block). As neurons could be more elaborated in higher or lower *z* planes, to ensure segmentation of cell somas we also used a *z*-stack of at least 100  $\mu\text{m}$  in depth centered on the focal plane for ROI selection. For each photostimulation triggered average we computed  $\Delta F/F_0$ , with  $F_0$  defined as the average fluorescence 1 s prior to photostimulation. We classified neurons as responsive if they showed a significant difference in their average fluorescence signal in a 100 ms window immediately after photostimulation compared with 100 ms baseline fluorescence immediately preceding photostimulation ( $p < 0.05$ , two-sample Student's *t* test).

### Targeted juxtacellular electrophysiology

*In vivo* juxtacellular recordings were performed during 2P imaging for guided access to olfactory bulb neurons. Recordings were performed with a Multiclamp 700b amplifier (Molecular Devices) and digitized at 20 kHz using an FPGA (National Instruments) and WaveSurfer software (Janelia Research Campus). Borosilicate glass pipettes were pulled to 5-11 M $\Omega$  (~1-1.5  $\mu\text{m}$  tip size) and filled with external solution (130 mM potassium gluconate, Millipore Sigma) containing fluorescent dye for visualization (Alexa 488/594 mixture, ThermoFisher Scientific). Before recordings, silicone plugs were removed from the cranial window and the dura was continuously perfused with sterile saline solution. After each recording session, holes in the cranial window were re-sealed using silicone elastomer, permitting multiple recording sessions for each animal.

Recordings were made exclusively from putative mitral cells. Latency of response was defined as the time from the onset of photostimulation to the first recorded spike. Latency values were averaged across photostimulations and neurons to compute the mean latency per condition. Jitter was defined as the standard deviation of the distribution of latencies across multiple trials for each individual neuron and condition, and was averaged across neurons to obtain the average jitter per photostimulation condition (Figures S4B and S4C).

### Network responses to photostimulation

Prior to behavioral training, we assessed the magnitude and specificity of photostimulation responses of individual mitral cells in the Tbet-cre mice included in the study. For each Tbet-cre mouse, we chose a FOV centered on the MCL that had a geometry allowing us to observe many (> 25) mitral cells simultaneously. We then targeted each mitral cell double-labeled with GCaMP6s and ChrimsonR-tdTomato for photostimulation individually and measured the response from each targeted neuron and the other mitral and non-mitral cells in the FOV. We used a higher average power for stimulation (30-45 mW) than used in behavioral training, delivered in a train of 3 pulses (10 ms on, 10 ms off) at 50 Hz. This was to ensure a clear division between responsive and unresponsive targeted neurons in a relatively small number of trials (30-60 trials), and to ensure robust responses despite differences in GCaMP6s expression. After photostimulating most observable double-labeled mitral cells, we chose a subset of cells with a significant average response (~40% of tested neurons) to be included in our set of neurons targeted for 2P photostimulation during behavioral training. We further analyzed the effect of individually photostimulating these responsive neurons on the averaged activity of other cells in the FOV (Figure 4).

We also analyzed population responses to simultaneous photostimulation of multiple MCs targeted in the behavioral experiments during blocks in which the maximum number of neurons were targeted for each animal (Figure S12). We selected blocks at the end of

training sessions when mice had ceased licking ( $[\text{Hits}+\text{FAs}] < 6$ , out of 60 trials), in order to exclude modulation due to behavioral factors. We analyzed how response distributions depended on distance from the targeted neurons using a nearest-neighbor analysis. For every neuron in the FOV we determined the distance to the nearest targeted MC. Neurons were then binned by distance (25  $\mu\text{m}$  bins) and we computed the median of the responses across neurons in each bin (Figure S12B). Responses were defined as the average of the normalized fluorescence during the 100 ms (3 frames) after photostimulation offset.

In both single and multiple mitral cell targeting experiments, chance level was determined by computing the average binned responses of the same neurons with stimulation times randomly chosen (shuffled) to account for correlations across neurons as well as activity trends that persisted across multiple photostimulations (Figures 4E and S12B, black curve).

### Behavioral training

All behavioral events (imaging time-stamping, respiration monitoring, stimulus delivery, water delivery, and lick detection) were monitored and controlled by custom programs written in Python (Voyeur software, <https://github.com/olfa-lab/Voyeur>) interfacing with a custom behavioral control system based on an Arduino Mega 2560 microcontroller (Smear et al., 2013). Photostimulation detection training began after at least 7 days of water restriction (1 ml/day), and at least 14 days after viral injection. Mice were housed on a reverse light/dark cycle, and training took place during the day. Training began with habituation to head-fixation (1–2 days), while animals were free to run on a 3D printed wheel. This was followed by water-sampling sessions (1–3 days) in which mice learned to lick a tube to receive 2  $\mu\text{l}$  droplets, until they learned to lick enough to receive the full 1 ml of water for the day. Licking was detected using a capacitive touch sensor (Sparkfun) coupled to hypodermic tubing which triggered the release of water droplets by a pinch valve.

Once the animals reliably licked for water, they were placed in a go/no-go photostimulation detection task in which they reported the presence or absence of one-photon (1P) photostimulation presented broadly to one hemisphere of the olfactory bulb. This training was used for shaping each animal's behavior prior to experiments probing detection of 2P ensemble photostimulation. This way, learning trajectories during 2P ensemble photostimulation would reflect each animal learning to detect activity in a small ensemble of neurons, and not an animal learning the contingencies of the go/no-go task. Photostimulation was delivered using a continuous wave diode laser (FTEC2, BLUE Sky Research) at 473 nm through a 105  $\mu\text{m}$  core diameter optic fiber (N.A. 0.22) placed over the cranial window at a 53° angle (~1.0 mm beam diameter at the brain surface). Animals performed a go/no-go task, in which 'go' (photostimulation) and 'no-go' (no photostimulation) trials were pseudo-randomly interleaved in a block structure (60 trials/block, 30 'go', ~600 trials/session). Each trial consisted of a pre-stimulus period (500 ms), stimulus period (20–70 ms), a delay (500 ms), response period (500 ms), and an inter-trial interval (ITI) with variable duration (5–7 s). On all trials, a broadband tone (piezo buzzer) and masking LEDs signaled the start of the pre-stimulus period and persisted through the stimulus period and delay. The masking LEDs were chosen such that the central wavelength matched that of the diode laser (473 nm) and were positioned near the animals' eyes to prevent detection based on visual cues. Offset of the tone and masking LEDs signaled the response period during which an animal could lick to receive a reward on "go" trials or withhold licking to avoid a punishment on "no-go" trials. Incorrect licking (false alarms) during the response period resulted in a tone from a second piezo buzzer of a different frequency (500 ms) and a 5 s "time-out" added to the ITI. During all other epochs animals were neither punished nor rewarded for licking, and after initial training mice generally did not lick outside of the response period.

Timing of photostimulation delivery was controlled in a closed-loop manner relative to sniff phase. Respiration was monitored using a pressure transducer coupled to a custom Teflon "odor port," which continuously passed filtered air over the mouse's nostrils at a rate of 0.5 l/min (Wilson et al., 2017). Pressure change relative to atmospheric pressure was measured using an externally mounted pressure sensor (24PCEFJ6G, Honeywell) positioned in front of the animal's nares. This pressure signal was amplified (AD620, Analog Devices), and a Schmitt (dual-threshold) trigger was used to define inhalation and exhalation onsets in real-time on an Arduino microcontroller. Once a "go" trial was initiated, the system detected the first inhalation onset and photostimulation was delivered at a fixed delay (onset = 20 or 40 ms) after inhalation by triggering the laser using a pulse generator. This timing corresponded roughly to the onset of the earliest odor driven responses reported by previous experiments (Shusterman et al., 2011), so this period was used to avoid interference from potentially uncontrolled olfactory stimulation.

During shaping, mice were initially trained to detect relatively strong 1P photostimulation (40 mW, 50 ms duration, 473 nm). Once performance for a given pulse energy exceeded 0.75 proportion correct, the pulse energy was systematically decreased until mice performed above 0.75 proportion correct at 1 mW for 1 ms duration for at least one block (except for one mouse who advanced after 1 mW for 2 ms). The fiber was positioned above the same hemisphere of the olfactory bulb across days, though not in the exact same position. In subsequent sessions, mice transitioned to detecting 2P photostimulation targeted to 11–27 neurons (Tbet-cre) or 30 neurons (WT) within the trained hemisphere (18–20 mW/patch, 10 ms duration), but not necessarily in the same volume illuminated during 1P training. These specific neurons were selected based on 1) co-expression of opsin and calcium indicator and 2) displaying a significant response to photostimulation averaged over  $\geq 30$  stimulus repetitions. All experimental timing and cues were identical to the shaping task, except that the masking LED was no longer used and the running wheel was immobilized to prevent vibration. Individually targeted neurons were held constant across days and confirmed to be responsive to photostimulation outside of the behavioral task prior to training. Mice performed 400–600 trials per session in blocks of 60 trials (30 'go'). All experimental manipulations varying the number, timing and efficacy of stimuli were interleaved as blocks of probe trials delivered to fully trained mice and were not explicitly used for training.

### Assessment of detection thresholds

Once performance on the 2P photostimulation detection task plateaued, animals were tested on detection accuracy as a function of the number of targeted neurons. In this experiment ‘reduced’ holograms were generated by progressively removing targets from the trained pattern (5–10 holograms depending on the maximum number of cells). The laser power was adjusted for each hologram to keep the average power per cell constant: 18–20 mW/patch. Removed targets were chosen at random without replacement within each session. Across sessions (1–5 per mouse), the target removal order was randomized. Detection accuracy was tested by pseudo-randomly interleaving blocks of each reduced hologram (60 trials/block, 30 ‘go’ trials). To determine each mouse’s sensitivity to the number of targeted neurons, psychometric performance curves were fit using a Weibull function and maximum likelihood estimation. Error bars for parameter estimates were generated using a bootstrap analysis.

### Manipulation of stimulus timing

To test the dependence of detection on the synchrony of photostimulation across neurons we rapidly switched between two or three holograms each representing a half or a third of the neurons on asynchronous stimulus blocks. To ensure that changes in detection were due to changes in stimulus synchrony, we first measured the switching time between the specific holograms used in these blocks of trials prior to each session. This was done by measuring the power at the sample (average power of the hologram) using a power meter (Thorlabs), while switching between holograms and observing the amount of time necessary for power to reach a stable asymptotic value after each switch. We observed that average power returned to 95% of its peak value after ~5–7 ms, depending on the specific holograms. To ensure that hologram efficiency was fully recovered before each stimulus presentation we conservatively set the time between photostimulations to be 10 ms.

### Optical sham-stimulation control

To confirm that detection relied on the spiking of neurons, and not confounding factors, animals were also tested on a control “sham stimulation” condition. The control stimulus was achieved by increasing the photostimulation pulse width from ~200 fs, to > 15 ps by adjusting the laser’s compressor. The laser’s average power (and therefore the delivered heat and indirect sensory effects that might be evoked) was held fixed. Mice experienced blocks of the sham stimulation interleaved with blocks of normal stimulation during the go/no-go stimulation detection task after the task had been learned (> 75% detection accuracy, WT mice; or 4 training sessions, Tbet-cre mice).

## QUANTIFICATION AND STATISTICAL ANALYSIS

Performance during behavior experiments was analyzed using custom-written MATLAB programs with detection accuracy quantified as the proportion of trials with correct responses ( $(\text{hits} + \text{correct rejects})/\text{total trials}$ ). No method was used to predetermine sample sizes. All statistical comparisons of behavioral and physiology data were performed using MATLAB and standard functions (ttest, fishertest, kruskalwallis, etc). Specific analyses are described alongside experiments in the text and figure captions.

**Neuron, Volume 108**

**Supplemental Information**

**Precise Holographic Manipulation  
of Olfactory Circuits Reveals Coding  
Features Determining Perceptual Detection**

**Jonathan V. Gill, Gilad M. Lerman, Hetince Zhao, Benjamin J. Stetler, Dmitry Rinberg, and Shy Shoham**

## Supplemental Information

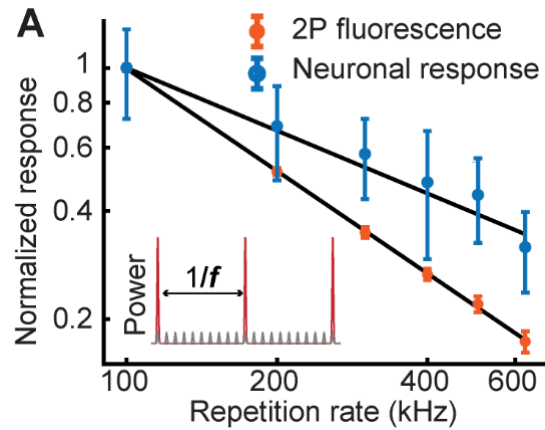


**Figure S1. Characterization of 2P excitation dependence on repetition rate.** (related to Figure 1) Evoked 2P fluorescence signal measured using fluorescein, and neuronal GCaMP6s responses as a function of the laser's repetition rate for a constant average power (mean  $\Delta F/F \pm$  SEM,  $n = 10$  cells, 1 WT mouse, 30 stimulations per rep. rate). The data is normalized to the mean response value at the lowest repetition rate. Inset shows a schematic of the laser pulses for high and low repetition rates.

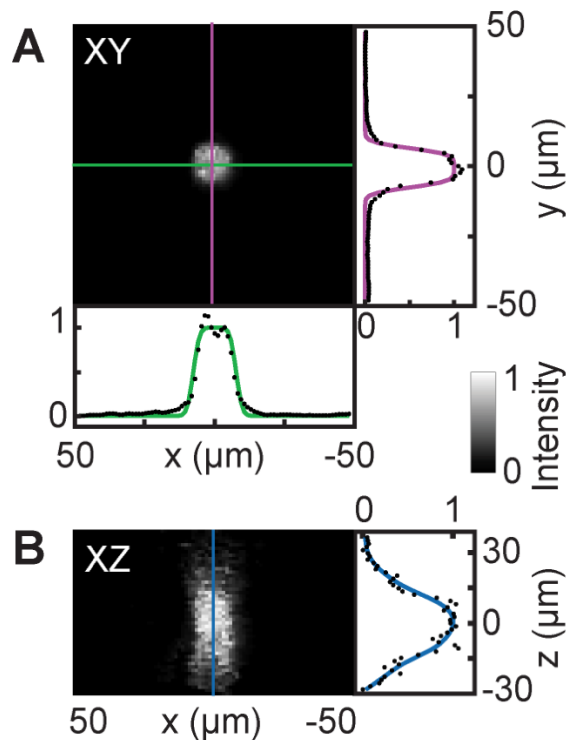


**Figure S2. Photostimulation point spread function.** (related to Figure 1) **A-B.** Light patches generated using the weighted Gerchberg-Saxton algorithm (Gerchberg and Saxton, 1972; Golan et al., 2009) were characterized using a widefield microscope. A thin ( $<5 \mu\text{m}$ ) fluorescein layer was illuminated with a light patch and the 2P excited fluorescence signal was projected onto a CMOS camera. **A.** Normalized fluorescence intensity in the  $(x,y)$  plane at the focus ( $z = 0$ ). The photostimulation point spread function measured 13  $\mu\text{m}$  and 12.8  $\mu\text{m}$  full width at half maximum (FWHM) in the  $x$  and  $y$  dimensions. A top-hat function convolved with a Gaussian kernel was fit to the data for visualization. **B.** Normalized fluorescence intensity in the  $(x,z)$  plane ( $y = 0$ ). The photostimulation point spread function measured 24.6  $\mu\text{m}$  FWHM in the  $z$  dimension. Fluorescence values were fit with a cubic smoothing spline for visualization.

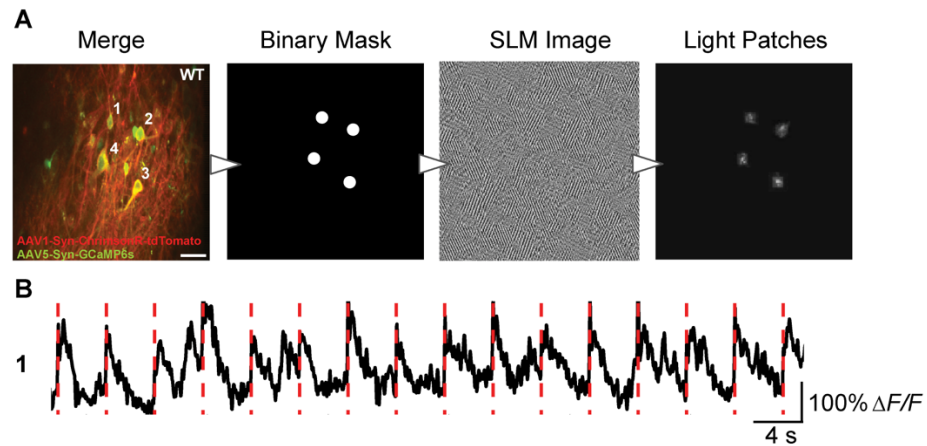


**Figure S3. Holographically targeting multiple neurons with light patches.** (related to Figure 1) **A.** Illustration of workflow for holographically targeting light patches to multiple neurons. Scale bar, 30  $\mu\text{m}$ . **B.** Example trial-by-trial calcium response to photostimulation for one neuron (4 targeted neurons, 50 ms photostimulation, 16 trials, 0.1  $\text{mW}/\mu\text{m}^2$ ,  $n = 1$  WT mouse).

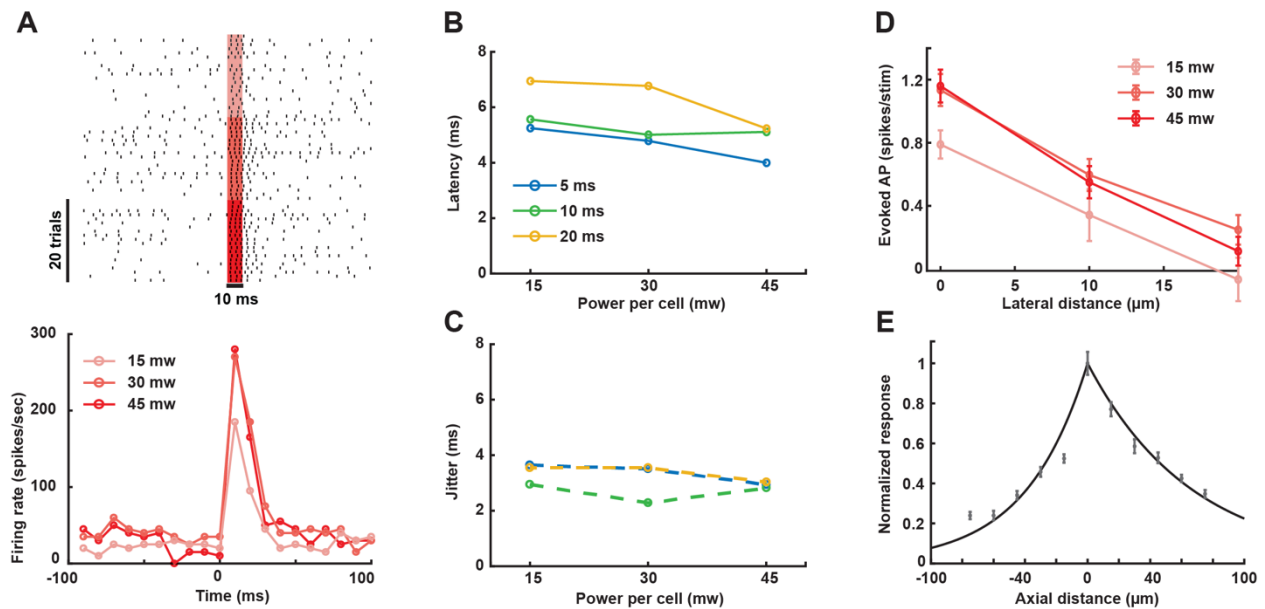


**Figure S4. Electrophysiological characterization of photostimulation.** (related to Figure 1) **A.** Example raster plots (top) and correspondent peristimulus time histograms (PSTHs) (bottom) for different stimulation powers, (red shading, photostimulation on;  $n = 1$  cell, 1 WT mouse, 20 trials per condition). **B-C.** The average latency (**B**) and jitter (**C**) of evoked spikes as a function of power per cell for different stimulation durations. The latency is defined as the time from photostimulation onset to the first spike within a 20 ms window, and jitter is defined as the average of the standard deviation of the latency across trials and cells ( $n = 5$  cells, 5 WT mice). **D-E.** The efficiency of photostimulation when moving the light patch away from the cell's soma laterally (**D**, mean  $\pm$  SEM,  $n = 4$  cells, 4 WT mice) and along the z-axis (**E**, mean  $\pm$  SEM,  $n = 9$  cells, 3 WT mice, 30 mW/patch, 0.19 mW/ $\mu\text{m}^2$ ).

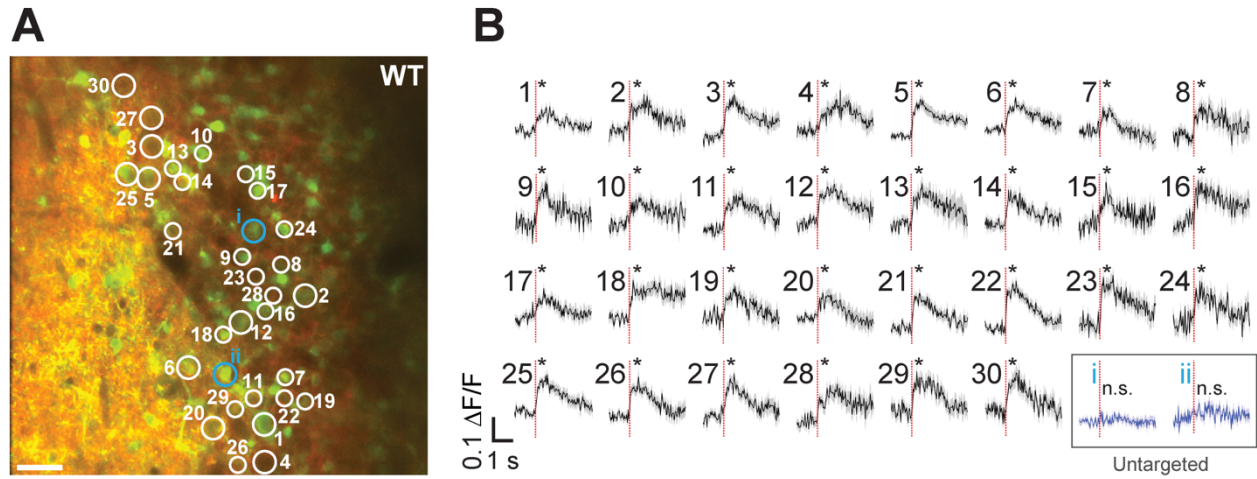


**Figure S5. All-optical control of 30 neurons.** (related to Figure 1) **A.** Thirty neurons were targeted for simultaneous 2P photostimulation (white circles) and 2P imaging (scale bar, 40  $\mu\text{m}$ ). **B.** Average GCaMP6s calcium response to photostimulation (red dashed line – stimulation onset) for 30 targeted neurons (black) and 2 example non-targeted neurons (blue) (mean  $\Delta F/F \pm \text{SEM}$ ,  $*p < 0.05$ , two-sample t-test, 30 trials, 10 ms stimulation duration, 18 mW/patch, 0.1 mW/ $\mu\text{m}^2$ ,  $n = 1$  WT mouse).

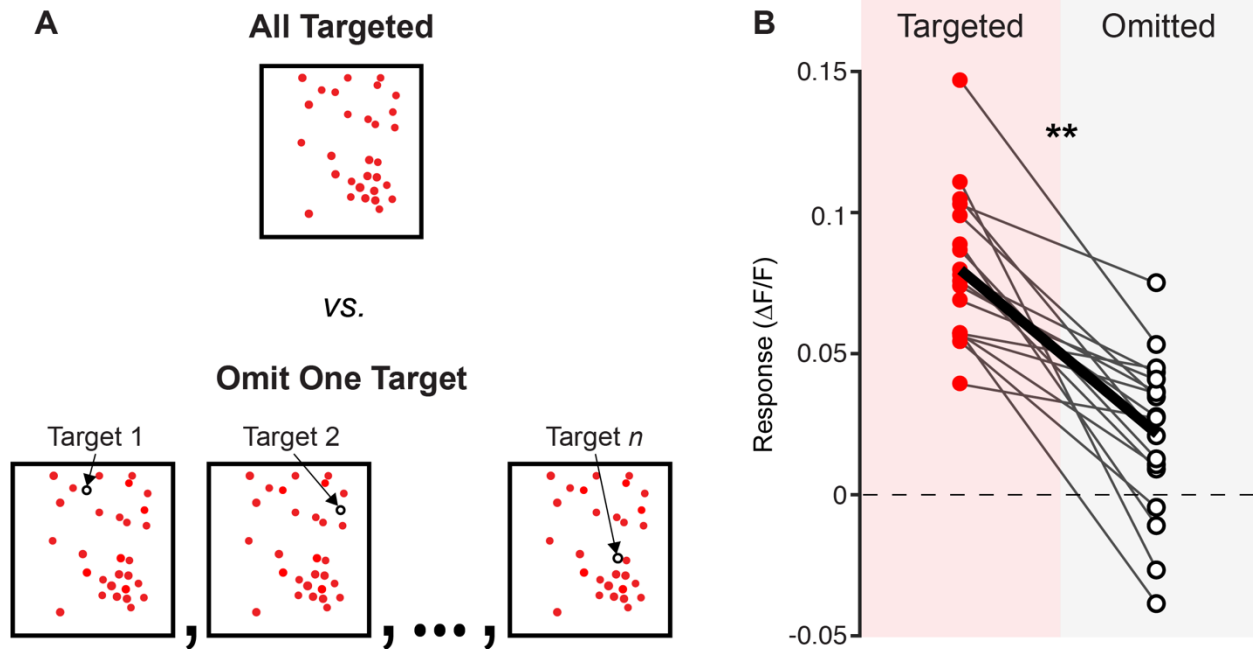


**Figure S6. Characterizing response in omitted photostimulation targets.** (related to Figure 1) **A.** Schematic of the omit-one-target experiment. Top. Pattern of spots targeting many neurons simultaneously. Bottom. Omit one target condition in which one of the spots is removed from the stimulation pattern. All spots are individually dropped, and the holograms are randomly presented to the mouse along with the all targeted hologram. **B.** Average response to 10 ms photostimulation. The average response per cell when it was targeted vs. when it was omitted with all other cells targeted. (\*\* $p < 0.001$ , two-sample t-test, Targeted:  $0.08 \pm 0.006$ , vs. Omitted:  $0.02 \pm 0.007$ , mean  $\Delta F/F \pm \text{SEM}$ , 28 targeted cells (19 responsive),  $n = 2$  WT mice, 30 photostimulations per datapoint, 10 ms duration, 20 mW/patch,  $0.125 \text{ mW}/\mu\text{m}^2$ ).

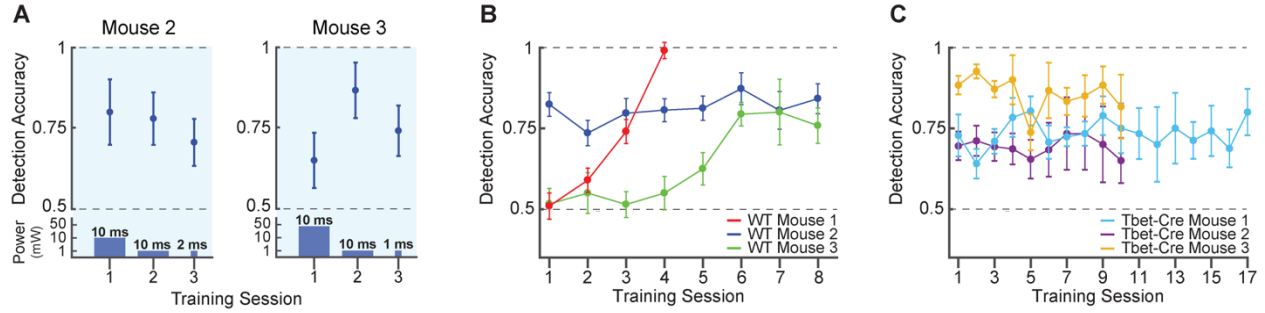


**Figure S7. Photostimulation detection training.** (related to Figure 2) **A.** Performance for 1-photon photostimulation detection training for individual mice. 1-photon photostimulation energy was decreased from session to session (mean  $\pm$  95% confidence intervals). Power and duration of 1-photon stimulation is schematized at the bottom of the graph. **B.** Performance for 2P photostimulation detection of the same 30 neurons (mitral and granule cells) across sessions (mean  $\pm$  95% confidence intervals,  $n = 3$  WT mice, 0.1-0.125 mW/ $\mu\text{m}^2$ ). All mice reached a performance  $>75\%$  correct within 7 sessions. **C.** Detection accuracy of 2P photostimulation targeting the same mitral cells across sessions in Tbet-Cre mice (mean  $\pm$  95% confidence intervals,  $n = 3$  Tbet-Cre mice, 0.1-0.15 mW/ $\mu\text{m}^2$ ). The number of mitral cells targeted was 17, 11 and 27 in mouse 1, 2 and 3, respectively.

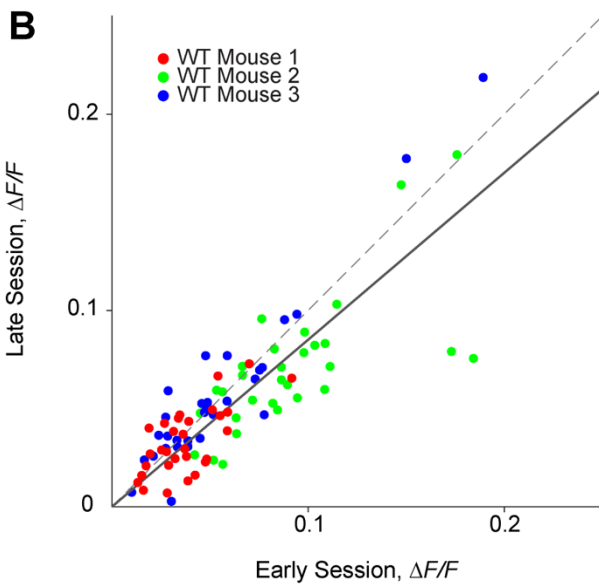
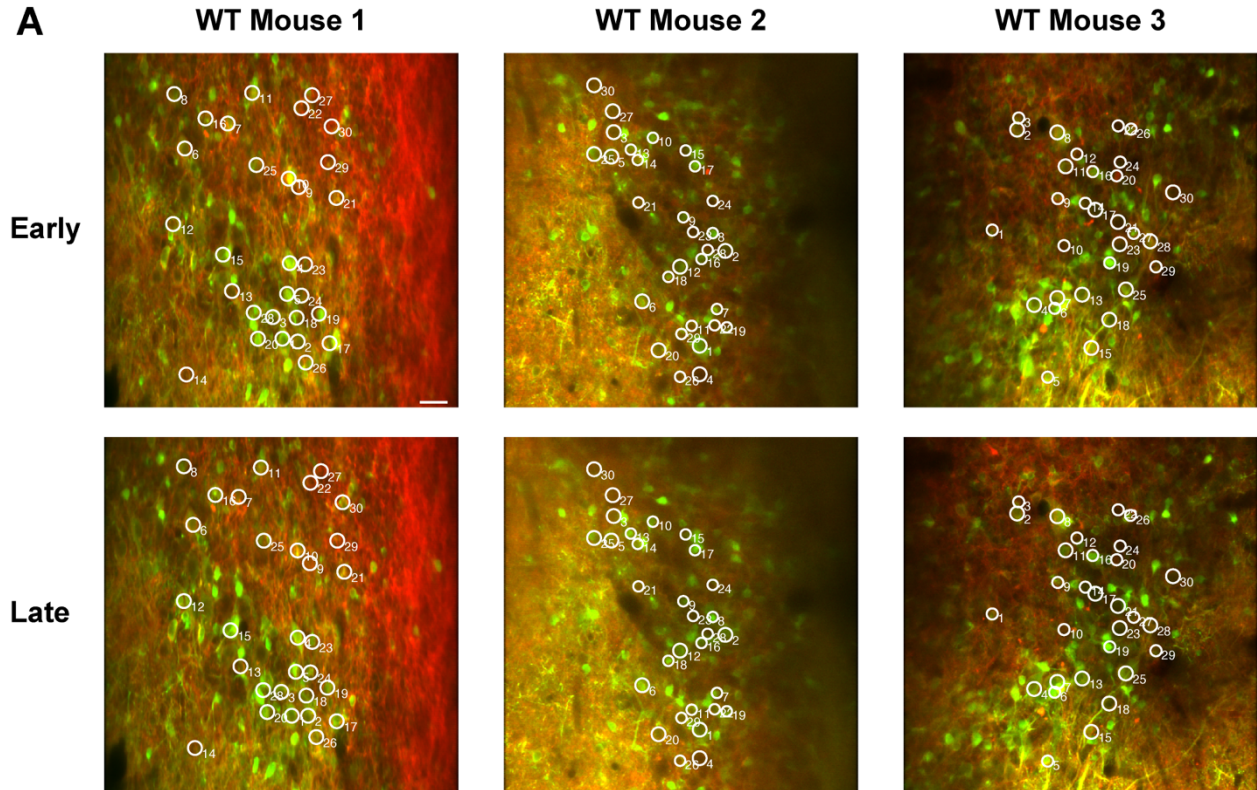


**Figure S8. Stability of neuronal targeting and responses across sessions.** (related to Figure 2)  
**A.** Example fields of view and targeted neurons (white circles) imaged early in training (upper) or late in training (lower) for three WT mice. ChrimsonR-tdTomato expression is shown in red, GCaMP6s expression in green. Scalebar = 30  $\mu\text{m}$ . **B.** Mean response to photostimulation was highly correlated across sessions (30 trials per session, 10 ms stimulation duration,  $n = 3$  WT mice, 0.1  $\text{mW}/\mu\text{m}^2$ ). Data points represent  $\Delta F/F$  values averaged over 330 ms following stimulation. Dashed line is the unity line and the solid line is the linear fit (slope = 0.85).

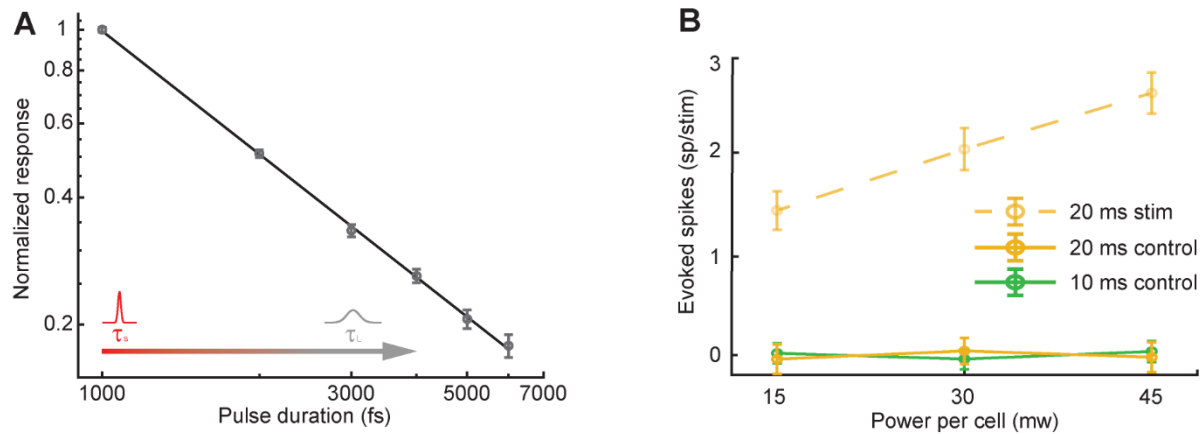


**Figure S9. Pulse duration effects characterization.** (related to Figure 3) **A.** Normalized excited 2P fluorescence in fluorescein as a function of pulse width (mean  $\Delta F/F \pm$  SEM). **B.** Average number of spikes evoked by long-pulse (solid line) and short pulse (dashed line) photostimulations. There was no significant change in the number of evoked spikes compared to baseline (mean  $\pm$  SEM,  $p = 0.99$ , Wilcoxon rank-sum test,  $n = 4$  cells, 4 WT mice).

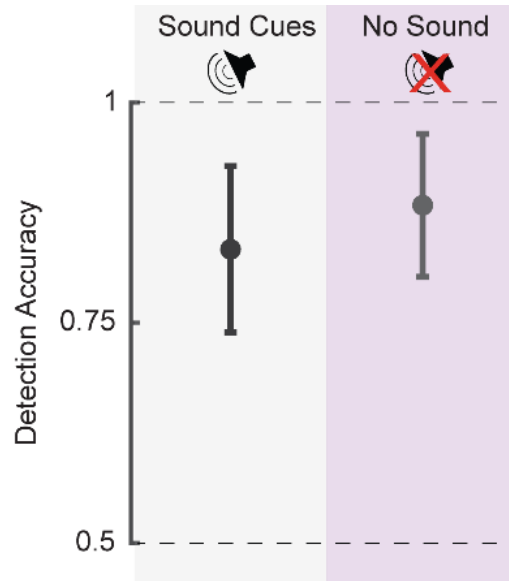
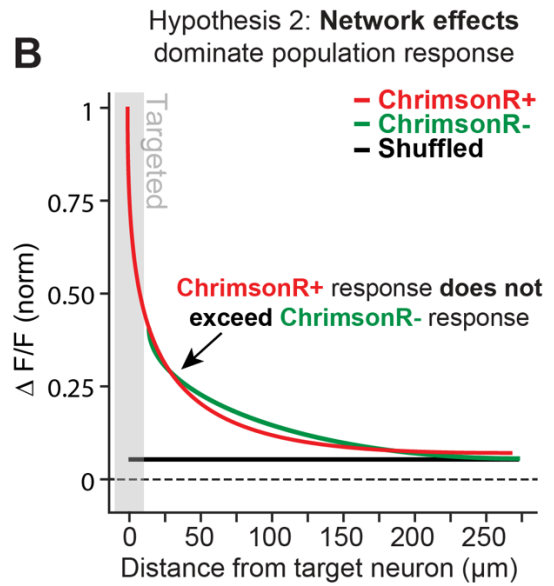
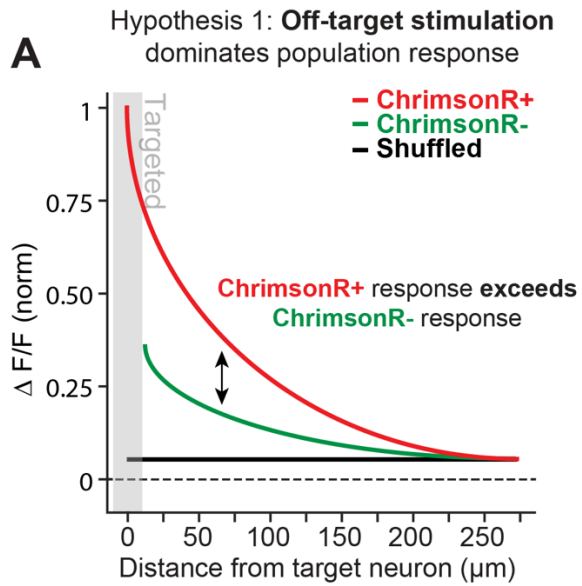


**Figure S10. Detection in the absence of sound cues.** (related to Figure 3) Detection accuracy in two sequential blocks of trials where sound cues were either present or omitted (error bars =  $\pm$  95% confidence intervals,  $p = 0.6$ , Fisher's exact test, 27 targeted mitral cells, 60 trials/data point, 20 mW/patch, 0.125 mW/ $\mu\text{m}^2$ ,  $n = 1$  Tbet-cre mouse).

## Single-Cell photostimulation response predictions



## Multiple-Cell photostimulation response predictions

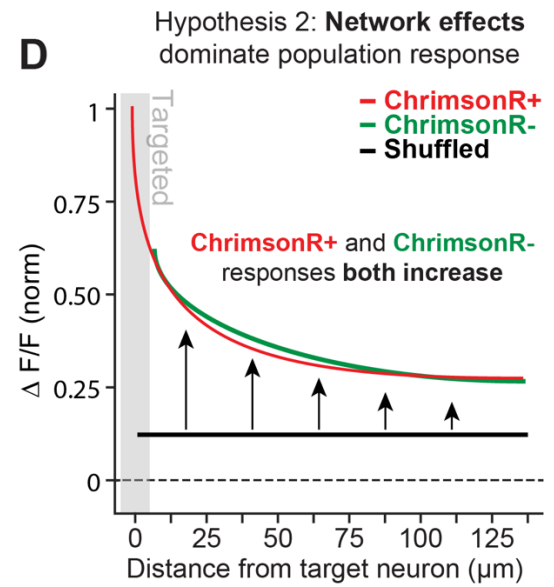
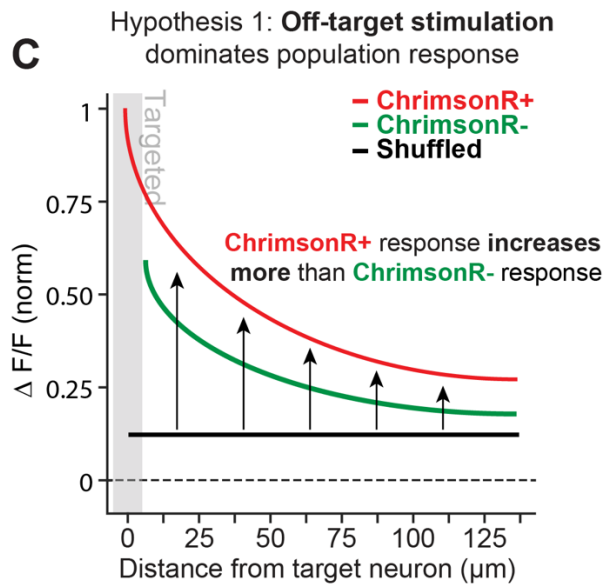


**Figure S11. Expected effects on population responses as a function of eccentricity from targeted neurons.** (related to Figure 4) **A-D.** Schematic of possible response profiles for opsin-positive/negative (ChrimsonR+, ChrimsonR-) neurons in Tbet-cre mice as a function of eccentricity from photostimulation targeted neurons under different degrees of off-target (accidental) or network (synaptically) driven activations. Red and green curves represent the mean response across cell types (ChrimsonR+, ChrimsonR-) at different radial eccentricities from targeted neurons. Shuffled curves represent the mean response of both ChrimsonR+ and ChrimsonR- neurons to randomly selected intervals during blocks of photostimulation trials. **A.** Expected outcome if photostimulation activates neighboring ChrimsonR+ neurons due to off-target photostimulation: ChrimsonR+ responses will exceed the of ChrimsonR- responses reflecting inadvertent stimulation of nearby Chrimson+ neurons. **B.** Expected outcome if single-cell photostimulation led to responses of nearby neurons due to network effects: ChrimsonR+ responses lack (the inadvertent) excess excitation and would not exceed the responses of ChrimsonR- neurons. **C-D.** During multiple-cell photostimulation, network mediated modulation of nearby neurons is expected to increase relative to single-cell photostimulation, leading to an upward shift in population response across eccentricities. **C.** If off-target photostimulation effects increase with an increase in the number of targeted neurons, ChrimsonR+ responses should increase more than ChrimsonR- responses. **D.** If network effects increase with the number of targeted neurons, but not off-target photostimulation, ChrimsonR+ and ChrimsonR- neurons should both similarly increase their responses across eccentricities.

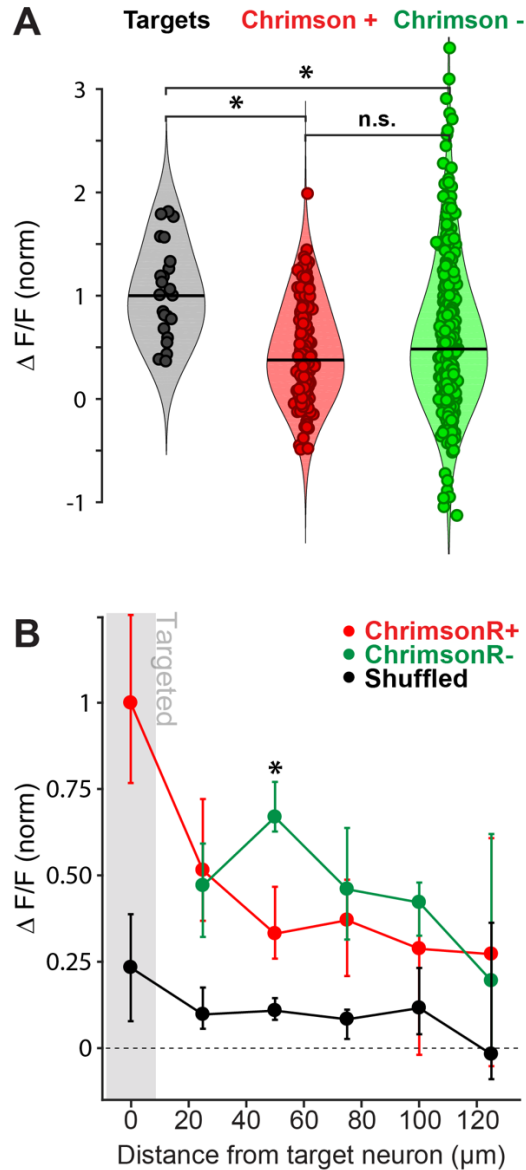


**Figure S12. Distribution of responses during photostimulation of multiple targets.** (related to Figure 4) **A.** Distribution of average responses in targeted mitral cells and untargeted opsin-positive (ChrimsonR+) and opsin-negative (ChrimsonR-) neurons following photostimulation of multiple neurons (black bars = median,  $*p < 0.05$ , Wilcoxon rank-sum test, 11-27 MCs targeted simultaneously, 183 Chrimson+ and 369 Chrimson- neurons,  $n = 3$  Tbet-cre mice, 20 mW/patch, 0.125 mW/ $\mu\text{m}^2$ , data normalized to median target response). **B.** Response as a function of opsin expression and eccentricity from targeted mitral cells (median  $\pm$  95% confidence intervals,  $*p < 0.05$ , ChrimsonR+ vs. ChrimsonR-, Wilcoxon rank-sum test, Holm-Bonferroni corrected for multiple comparisons,  $n = 3$  Tbet-cre mice, 20 mW/patch, 0.125 mW/ $\mu\text{m}^2$ , data normalized to median target response). Shuffled data corresponds to the distribution of binned responses of the same neurons with stimulation times randomly chosen (see STAR Methods).

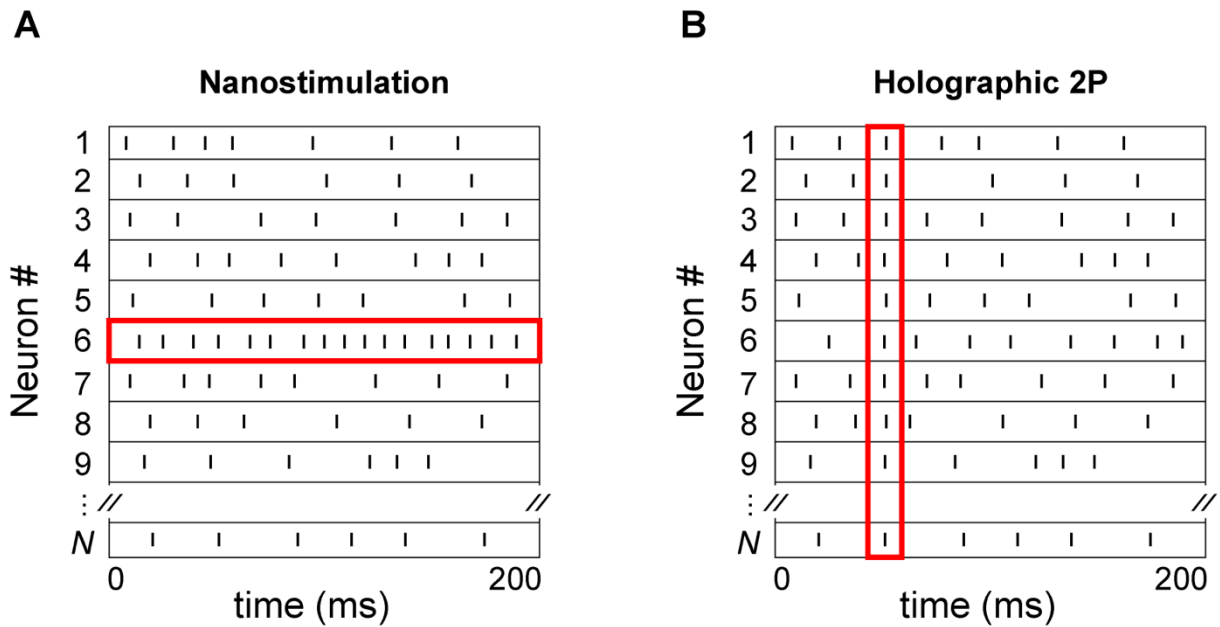


**Figure S13. Experimental paradigms exploring different modes of spike detectability.** (related to Figure 5) **A-B.** Nanostimulation and holographic 2P photostimulation address different and complementary coding strategies. **A.** Nanostimulation explores detection sensitivity to increases in the spike rate of individual neurons over 100s of milliseconds **B.** Holographic 2P photostimulation explores detection sensitivity to spikes coordinated across individually selected neurons on a timescale of <10 ms.